Birefringent Cavity for CQED

Thesis by

Yat Shan Au

In Partial Fulfillment of the Requirements

for the Degree of

Bachelor of Science

California Institute of Technology

Pasadena, California

2006

(Defended May 8, 2006)

Acknowledgements

I would like to thank Takao Aoki, Travis Bannerman, Kaushik Bhattacharya, Kevin Birnbaum, Andreea Boca, David Boozer, Warwick Bowen, Toby Burrows, Chin-Wen Chou, Hugues de Riedmatten, Matt Eichenfield, Daniel Felinto, Tony Gross, Jeff Kimble, Russell Miller, Tracy Northup, Andrey Rodionov, Elizabeth Wilcut and Dalziel Wilson for their continuous support, helpful discussions and encouragement. This work was supported by the Physics Department and the Student-Faculty Programs at the California Institute of Technology.

Abstract

By trapping a single atom in a Fabry-Perot cavity, we can realize strong coupling between the atom and the electromagnetic field, which may in the future be utilized to perform quantum gates in quantum computing. Previous experiments with Cesium atoms at the Caltech Quantum Optics group achieved a trapping time of 3 seconds, and they led to a detailed study of the atom-photon interactions known as the vacuum-Rabi splitting. It is believed that the trapping time is limited by collisions with residual gas molecules inside the vacuum chamber. I report three designs for the piezoelectric-controlled cavity mirror mount, bakeable to a temperature above 250 °C and hence more desirable for deployments in ultra-high vacuum (UHV). I also present new procedures which I have helped to develop for cavity construction and the characterization of cavities. In addition, I consider cavity birefringence, which can present complications to our experiments because a birefringent cavity supports two orthogonal, nondegenerate modes. I developed a simple model of cavity birefringence and made our first attempt to actively induce birefringence by stressing the cavity mirrors with piezoelectric materials, although we have not yet been able to demonstrate control over cavity birefringence. Nonetheless, with expected improvements in both mechanical stability of the cavity and base pressure of the system, it is hoped that a longer trapping time of 30 seconds can be achieved and that the new experiment with a single-sided cavity can lead to further studies of the dynamics of atom-photon interactions.

Contents

List of Figures

List of Tables

Chapter 1

Introduction and Motivation

1.1 Introduction

Despite that the laws of physics governing the microscopic and macroscopic worlds are identical, the behavior of matter at the atomic level is drastically different from our observations of the macroscopic world. For instance, atoms do not possess well-defined positions and momenta, although these are quantities we can measure macroscopically. Atomic behaviors are governed by quantum mechanics, in which an atom is described by its wavefunction and a system is characterized by its Hamiltonian. A wavefunction can be expanded as a linear combination of the eigenstates of the Hamiltonian. When a measurement is made on an atom, its wavefunction collapses probabilistically into one of the eigenstates of the Hamiltonian. It is probabilistic behavior that distinguishes quantum effects from classical effects [1]. The quantum mechanical behaviors of simple systems such as "the single particle in a box" are relatively easy to understand in theory, but their experimental realizations are much more difficult tasks.

Although the building blocks of matter are governed by quantum mechanics, quantum mechanical effects are not usually observed in the real world. Quantum mechanical effects are concealed by a process known as "decoherence." Atoms are not isolated from one another, but instead they are constantly interacting with the environment. These interactions are effectively continuous measurements on the atom. These measurements keep the atom in an eigenstate, and as a result, there is no probabilistic

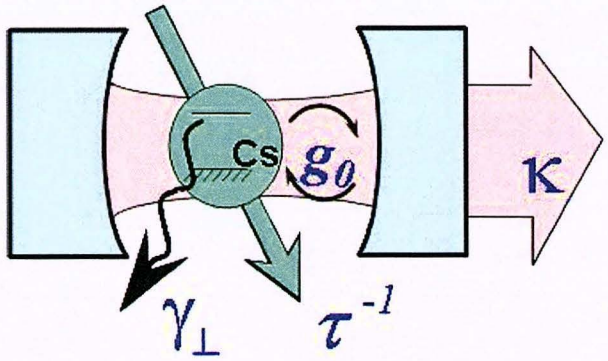

Figure 1.1: Characteristic parameters of our cavity QED system: g_0, one half the Rabi frequency for the coupling between the atom and the cavity field; κ, the cavity - field decay rate; γ, the atomic spontaneous emission rate; τ, the transit time of an atom through the cavity. Strong coupling requires $g_0 >> max\{\kappa, \gamma, 1/\tau\}$ [3].

collapse of the wavefunction when we make a measurement. Therefore, the results of physical measurements are indistinguishable from that of a classical system [2].

1.2 Strong coupling

In order to observe and eventually to manipulate quantum mechanical systems, we consider approximately isolated systems of single quanta. In these systems, the interactions with the environment are minimized. The strength of interactions can be measured by the rates at which the system exchanges energy. A system is in the regime of "strong coupling" when the rate of energy exchange among particles within the system is much faster than the energy dissipation rate to the environment. One of the experimental realizations of strong coupling is cavity quantum electrodynamics (cavity QED). In cavity QED, an atom can be strongly coupled to the electromagnetic mode of a resonator, for instance, an optical cavity (Fig. 1.1). The dipole moment of the atom and the electromagnetic modes within the cavity combine together to form a system of single quanta [3].

The first experimental observation of atom-cavity strong coupling in optical cavity

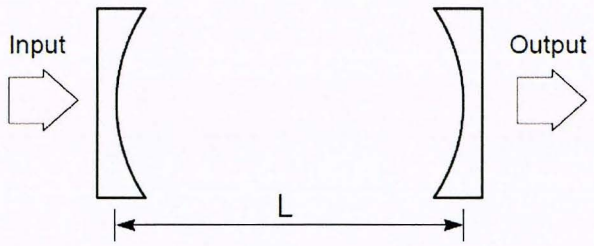

Figure 1.2: A simplified schematic of a Fabry-Perot resonator [8].

QED was made in 1992 by averaging measurements over a series of single atoms from a thermal atomic beam traversing the cavity [4]. When laser-cooled atoms instead of a thermal beam are used, measurements of single atoms can be made one at a time, in real-time [5]. (There are physical systems for studying cavity QED other than the optical cavity that we use. For example, the Haroche group at l'Ecole Normale Supérieure in Paris studies Rydberg atoms with microwave cavities [6]; the Schoelkopf group at Yale University employs solid-state resonators and Josephson junctions [7].)

1.3 Optical cavity

The optical cavity used in experiments in the Caltech Quantum Optics group is a Fabry-Perot resonator, which consists of two highly reflective spherical mirrors separated by a fixed distance L (Fig. 1.2). The cavity defines a set of electromagnetic field modes in both frequency and physical space. These modes comprise both longitudinal and transverse modes. The longitudinal modes are separated in frequency by a free spectral range (FSR) of $c/2L$, where c is the speed of light. A Fabry-Perot cavity is characterized by its finesse

$$F = \frac{\pi}{T_1 + T_2 + A_1 + A_2} = \frac{\Delta\nu_{FSR}}{\Delta\nu_{fwhm}} \tag{1.1}$$

$$Q = \frac{2d}{\lambda}F = (Number\ of\ half\ wavelengths) \cdot Finesse \tag{1.2}$$

where T_1, T_2 (A_1, A_2) is the power transmission (power loss due to scattering and absorption) of mirror 1 and mirror 2 respectively, $\Delta\nu_{FSR}$ is the free spectral range, $\Delta\nu_{fwhm}$ is the cavity linewidth and Q is the quality factor [9]. Note that Eq. 1.1 only applies to ideal high-finesse cavities made of mirrors of high reflectivity.

In order to achieve strong coupling, the electric field acting on the atom has to be maximized while keeping the number of photons within the cavity small ($\sim$ 1 photon). The cavity length L and the finesse F are two important parameters. The TEM_{00} mode of a laser has a Gaussian profile. By having a short cavity ($L \approx$ 40 μm) whose mirrors have a steep radius of curvature, the waist of the laser beam is small and hence the resulting electric field acting on the atom is strong (small mode volume). Furthermore, using mirrors with high finesse, photon loss and hence number of photons within the cavity can be minimized. In current experiments in the Kimble group, custom-made mirrors ($F \approx 4.8 \times 10^5$) of extremely low loss are employed [3]. The state of the art in low-loss mirrors corresponds to a cavity finesse of 1.9×10^6 [10], and ongoing collaborations between our group and the mirror manufacturers are trying to push this figure even higher.

1.4 Cavity QED

When a single atom is trapped inside the optical cavity, a coherent coupling between the atom and the cavity field is created through atomic dipole interactions. In the simplest theoretical model, the atom-cavity system is described by the Schrödinger equation with the Jaynes-Cummings Hamiltonian [11],

$$H_{JC} = \hbar\omega\hat{a}^\dagger\hat{a} + \hbar\omega\hat{\sigma}^\dagger\hat{\sigma} + \hbar g_0(\hat{a}\hat{\sigma}^\dagger + \hat{a}^\dagger\hat{\sigma}), \tag{1.3}$$

where ($\hat{\sigma}^\dagger$,$\hat{\sigma}$) and ($\hat{a}^\dagger$,$\hat{a}$) are the creation and annihilation operators for the dipole and cavity modes respectively, g_0 is one half of the single-photon Rabi frequency and ω is the common resonance frequency of both atom and cavity.

If $|g, n\rangle$ and $|e, n-1\rangle$ denote the atomic ground state with n photons and the

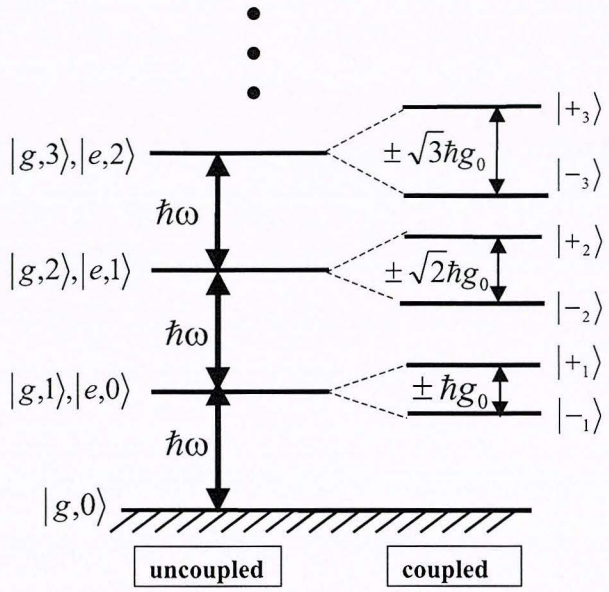

Figure 1.3: Jaynes-Cummings eigenstates for a degenerate atom and cavity [3].

excited atomic state with $n-1$ photons respectively, the coupled eigenstates and eigenvalues are given by (Fig. 1.3)

$$|\pm_n\rangle = \frac{1}{\sqrt{2}}(|g,n\rangle \pm |e,n-1\rangle) \tag{1.4}$$

$$E_{\pm_n} = n\hbar\omega \pm \sqrt{n}\hbar g_0. \tag{1.5}$$

The spectrum of the Jaynes-Cummings Hamiltonian is observed through an effect known as vacuum-Rabi splitting. The Lorentzian line profile of the empty cavity becomes a double-peaked transmission function in the presence of strong atom-cavity coupling, when driven by a weak probing field (Fig. 1.4). Since the Jaynes-Cummings Hamiltonian ignores energy dissipation to the environment, it cannot explain the details of the transmission function such as the widths of the two peaks. Nonetheless, more sophisticated theoretical models that introduce dissipation via a master equation are available to account for the details [12].

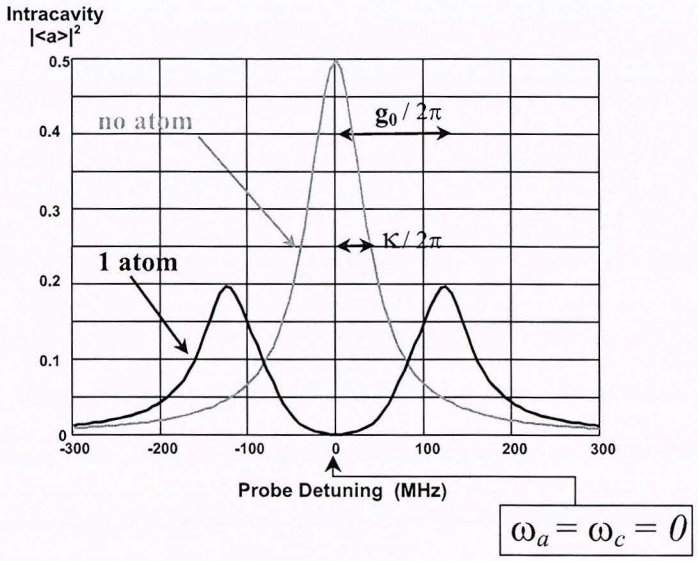

Figure 1.4: Vacuum-Rabi Splitting. The empty cavity single-peaked transmission line splits into two peaks [3].

1.5 CQED experiments with cold atoms

Cesium atoms used in experiments in the Quantum Optics group are confined and cooled in a magneto-optical trap (MOT) located directly above the optical cavity. A MOT is a region of space with its trapping potential formed by six counter-propagating red-detuned laser beams and a magnetic field gradient [14]. There are approximately 10^4 cesium atoms at 120 μK stored in the MOT, where 120 μK is a characteristic "Doppler temperature"of the cesium atoms [14]. In order to minimize the interactions between the cesium atoms and air molecules, the experiment is performed in ultrahigh vacuum (10^{-10} torr). The cesium atoms are allowed to escape from the MOT slowly. These atoms are further cooled to about 10–20 μ K with polarization gradient cooling [14] before they drop onto the cavity. Since the separation between the two cavity mirrors is very small (40 μm), the probability of having only one atom in the cavity at one time is much larger than that of multiple atoms. When an atom is inside the cavity, it couples strongly with the electromagnetic field through dipole interactions. The field of a probing beam along the cavity axis and coupled

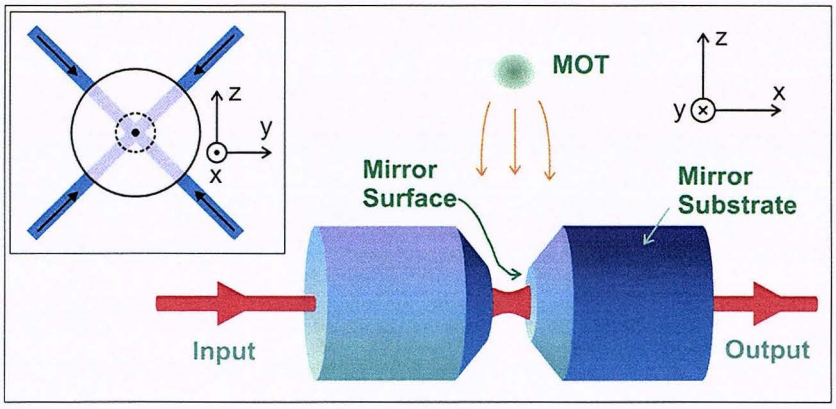

Figure 1.5: A simplified schematic of the experiment for trapping a single atom in an optical cavity in the regime of strong coupling [13].

to the cavity mode is spatially dependent and can be used to trap atoms in a cavity [15, 16]. In this experiment, the laser is used as both trapping and probing beam, and the trapping can be achieved for approximately 100 μs with an average field strength of less than one photon.

Another technique for trapping atoms employs a far-off-resonant trap (FORT) [14]. The working principle of a FORT is identical to that of an "optical tweezer,"in which the trapping force is provided by red-detuned laser beams. With the use of a FORT, current experiments in the Kimble group have achieved a trapping time of 3 s [13]. Our FORT (935 nm) is coupled to a different longitudinal mode of the cavity, and therefore, is built up by the cavity (Finesse $\sim$ 2000 at 935 nm). We are using a lower power ($\sim$ 1 mW) of input light, compared to other groups which apply their FORT from the sides [17, 18]. Once an atom is trapped, experiments such as the observation of vacuum-Rabi splitting for single atoms can be performed [19].

1.6 A new CQED experiment

The prospects of the study of cavity QED are promising. One recently proposed scheme for networked quantum computation comprises nodes connected by quantum

communication channels. At each node, quantum bits could be stored in an atom trapped in a cavity. The strong coupling between the trapped atom and the cavity could be utilized to perform quantum gates [20]. Networked quantum computation could lead to technological breakthroughs in both computation and communication.

In conjunction with simple single-qubit operations, quantum controlled phase-flip gate can realize universal quantum computing [21]. In order to implement the quantum controlled phase-flip gate in an atom-cavity system, we plan to construct our first single-sided cavity. In an ideal single-sided cavity, a photon enters and exits the cavity through the same mirror, and acquires a specific phase-shift in the process. Under certain conditions, the presence of an atom inside the cavity can prevent the entrance of a photon, resulting in a phase-shift different from the previous case. Therefore, we can control phase-shift of the exit photon with the presence or absence of an atom inside the cavity [21].

We are currently building a new vacuum chamber system, containing a new cavity in which atoms are trapped with a FORT. There are three major differences between past systems and this new one. First, the new cavity will be asymmetric: one of the cavity mirrors will be more transmissive than the other, so that the emission of the photons will primarily take place from one cavity mirror (i.e. a single-sided cavity). Second, birefringent splitting of the resonant cavity mode will be induced deliberately, instead of attempting to minimize it (as has been done for past cavities). Third, the target background pressure in the vacuum chamber will be 10^{-11} torr, which is ten times lower than in previous systems.

This thesis discusses these motivations in more detail, presents the redesign of the piezoelectric mirror mount, and describes the construction of test cavities and their characterizations.

1.7 My history in the group

I joined the Quantum Optics group in the spring of 2005, and I started working with graduate student Tracy Northup in lab 1. My first task was searching for better

vacuum materials, especially a bakeable piezoelectric that could be used to translate the cavity mirrors. I built a new cavity testing breadboard so that the original one could be shipped to the mirror manufacturer in Colorado for characterization of our custom-made mirrors. I also learned the hands-on techniques of an atomic physics lab and studied high-vacuum system construction. Over the summer, I was part of a team of three SURF students with Travis Bannerman and Toby Burrows. Travis was working on characterizations and improvements on the mechanical isolation system; Toby was working on inducing cavity birefringence; I was working on new designs of the piezoelectric mirror mounts. In the fall, graduate student Dalizel Wilson and I started the construction of test cavities. I also assisted in constructing the new chamber. After struggling with dusty mirrors for a couple months, we finally got our first cavity in December. In the winter of 2006, we built a cavity of chosen length and measured its finesse. We then started measurements on birefringent splittings of our cavities. I also worked on the Finite Element Analysis calculations of the strain pattern on the mirrors before my visits to graduate schools, while Dal was cracking more mirrors as he attempted to induce birefingence by stressing them mechanically.

1.8 Overview

In Chapter 2, I describe the various considerations in the design of the piezoelectric mirror mount and present three possible designs. Chapter 3 summarizes the procedures that we followed and developed for cavity construction. In Chapter 4, I describe the measurement of the cavity finesse. Chapter 5 discusses how to build a cavity of chosen length (to within ~ 500 nm). Chapter 6 presents our calculations on the strain pattern on our mirrors and measurements of the birefringent splittings. In Chapter 7, I make suggestions on future cavity constructions and describe the current state of the experiment.

Chapter 2

Design of Piezoelectric Mirror Mounts

2.1 Cavity redesign

The Fabry-Perot cavity used in current experiments at the Caltech Quantum Optics group [22] is composed of two mirrors on cylindrical substrates. The substrates are 4 mm long and 3 mm in diameter, tapered down to a 1 mm mirror face (Fig. 1.5) whose small size permits the construction of very small cavities. The mirrors are glued to piezoelectric transducers on the mount via V-blocks. The cavity length is precisely adjusted by two pieces of shear-mode piezoelectric material which translate the mirrors along the cavity axis.

The current cavity mirror mount imposed two majors limitations on our experiments. First, it is believe that the trapping time of the atom is limited by collisions with residual gas molecules inside the vacuum chamber [23]. Since the mirror mount could not be baked seriously, it is suspected to contribute to the outgassing rate of the vacuum chamber significantly. Second, the mirror mount induced birefringent splitting by stressing the mirrors [3], and birefringence can create complications for our experiments.

In order to achieve the goals for our new experiment outlined in Section 1.6, we have to redesign the mirror mount for the cavity. Three major considerations of this design are mechanical stability, vacuum compatibility and range of adjustment of the

cavity length. In the following section, I will discuss each of these considerations, why they need to be improved upon, and the solutions that I have proposed.

2.2 Mechanical stability

For the purpose of our experiment, the cavity length should be stable up to 10^{-14} m over the time of measurement [23]. In order to stabilize the cavity length, we first have to obtain very good passive mechanical stability, then apply active feedback to the piezos on which the mirrors are mounted. The feedback signal is provided by an auxiliary laser coupled to a higher-frequency longitudinal mode of the cavity. One way to achieve high mechanical stability passively is to keep most of the structure on a plane, as suggested by finite element analysis (FEA). In particular, the use of cylindrical piezos, which had been a part of past Kimble lab cavities, is better avoided [3]. Since the 1 mm thick piezo plate which we plan to use has its lowest resonant frequency around 60 kHz, our goal is to have the lowest resonant frequency above 60 kHz in our design.

In addition, undergraduate student Travis Bannerman is currently working on the characterizations and improvements of the mechanical isolation of the vacuum system as his senior thesis project.

2.3 Vacuum compatibility

Ultra-high vacuum compatibility imposes two restrictions on the design. First, the mirror mount can only be made of low outgassing materials. Outgassing refers to the spontaneous emission of gases from various materials inside the chamber, and it is a significant gas load for the vacuum pump at pressures below 0.1 torr [24]. Second, the mirror mount must be compatible with baking. Baking is the process in which the temperature of the vacuum chamber is raised while gas molecules are being pumped out of the chamber. Since the outgassing rate increases with temperature, baking reduces the time needed for depleting residual gases inside the vacuum chamber.

Vacuum Components	Max. Bakeable Temperature in °C
Caburn H27DUHV epoxy	270
Ferroperm Pz 23 & Pz 27 Piezos	250-300
Getter electrical feedthroughs	450
Ion pumps without magnets	350
Piezo electrical feedthrough	450
Residual gas analyzer (RGA)	300
Stainless nipples and flanges	450
Stainless steel chambers, upper and lower	450
Stainless tees, crosses, multiplexers	450
Titanium sublimation pump cartridge	350
Valves for roughing pumps	450 open, 350 closed
Windows, AR coated	400

Table 2.1: Bakeable temperature for various vacuum components. Note that the limit of baking is mainly imposed by the piezo and the epoxy.

It is not too difficult to meet the first requirement, as many metals (e.g. stainless steel and aluminum) have low outgassing rates. The real challenge is to transfer the motions of the piezo into a adjustment of the cavity length. We have two main options: adhering the mirrors onto the piezo with a minimum amount of glue (which tends to limit vacuum compatibility), or clamping the mirrors and the piezo onto the mount. I have considered attaching the piezo to the mount by soldering or mechanical bonding with gold foils, to minimize the use of glue. However, I found through experimental trials that the bondings are not strong enough in both cases. Instead, I located an ultra-high vacuum glue H27DUHV from Caburn MDC (West Sussex, U.K.), which is both vacuum-compatible up to 10^{-11} torr and bakeable up to 270 °C, and which we are currently planning to use.

The limit of baking is mainly imposed by the piezoelectric (Table. 2.1). Each type of piezoelectric material has a Curie temperature above which it becomes denatured through depolarization. The piezoelectric material can also be depolarized at lower temperature if it is heated for long enough. The piezoelectric material used in past Kimble lab cavities has a relatively low Curie temperature of 290 °C and it was not tested for serious baking above 120 °C. Due to considerations on birefringent splitting, past cavities were not baked above 40 °C [3]. We hope to improve the limitation

imposed by the piezoelectric, as we may not be too concerned about birefringent splitting in some future experiments [25]. In principle, we could always repolarize a depolarized piezo by applying a poling voltage across the two electrodes. However, according to American Piezo Ceramics Inc. (Mackeyville, PA), the poling voltage is about 3 kV per mil, which is prohibitively high for use in our experiment. Information on maximum baking temperatures and times for piezoelectric materials is not readily available, and these temperatures vary with the type of piezo. For instance, American Piezo Ceramics Inc. sells piezos that can only be baked up to half of the Curie temperature; Ferroperm Piezoceramics (Kvistgaard, Denmark) sells a piezo, Pz27, that has a Curie temperature of 350 °C, but its recommended maximum working temperature is 250 °C. One reliable way to learn about the bakeable temperature is to conduct our own tests.

I chose piezo plates Pz23 and Pz27 from Ferroperm Piezoceramics for our tests because of their large piezoelectric moduli ($d_{31} = 130$pm/V and $d_{15} = 335$pm/V for Pz23; $d_{31} = 170$pm/V and $d_{15} = 500$pm/V for Pz27) and high Curie temperature of 350 °C. Given an applied voltage, these piezoelectric moduli determine the distance traveled of a piezo, discussed further in section 2.4.

In order to determine the final baking temperature for our chamber, I considered the thermal desorption curve of stainless steel, the material of our chamber. Since stainless steel has a desorption peak for water molecules at approximately 300 °C (Fig. 2.1), we would like to bake our vacuum chamber at least up to that temperature. However, not all components of the vacuum chamber are bakeable to 300 °C; for instance, the UHV glue which we are planning to use is only bakeable up to 270 °C. Therefore, we plan to bake various components separately up to their maximum baking temperatures and assemble the chamber in a short amount of time after baking. The assembled chamber will then be baked at a more conservative temperature.

In the summer of 2005, I baked a Pz23 piezoelectric plate from Ferroperm Piezoceramics at 198 °C for about 48 hours. The baking temperature of our test was limited at the time by the maximum settings of our test oven, but we could bake at a much higher temperature with the large oven that we have since obtained. I did not notice

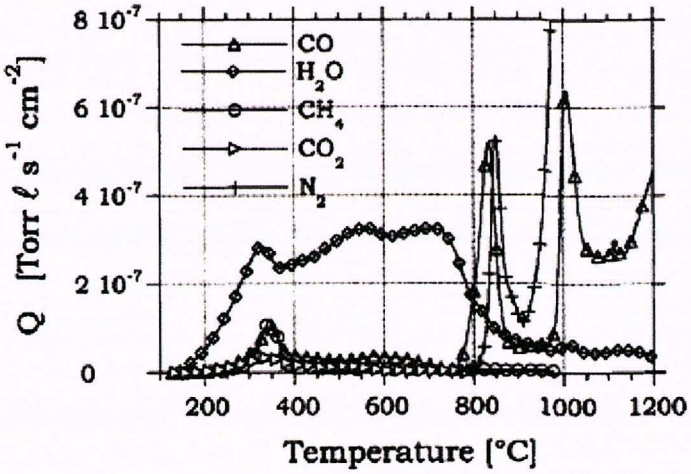

Figure 2.1: Thermal desorption spectra of 316LN electro slag remelting (ESR) processed steel [26]. Note that the composition of the outgassing molecules is very different from that of air and depends on the material, surface treatments, contaminants, temperature and history. For properly cleaned stainless steel and aluminum chambers, water accounts for 85% of the outgassing molecules at the beginning of a bake-out. Other important species are H_2, CO, CO_2 and CH_4. The sources of outgassing not only include molecules previouly absorbed onto the wall of the vacuum chamber, but also they include molecules generated by chemical reactions. For instance, water can be released from iron oxides on stainless steel: $Fe_xO_y + 2H \rightarrow Fe + H_2O$, with an activation energy of 80 to 92 kJ/mol [27]. Therefore, a baking temperature of 100 °C is insufficient for reducing the outgassing rate of water molecules. Since stainless steel has a desorption peak for water molecules at approximately 300 °C, we would like to bake our vacuum chamber at least up to that temperature.

any changes as a result of baking in the piezoelectric modulus d_{31}, as inferred from the measurement of the length of travel. However, some components of the electrical connection, such as solder, melt in the baking process. Since the final baking temperature may be 100 °C higher, more tests on the piezo and other electrical components will be conducted using the large oven.

2.4 Tunable range of the cavity

The cavity resonances occur only when $n\lambda/2$ wavelengths fit inside the cavity. Since the $6S_{1/2}, F = 4 \rightarrow 6P_{3/2}, F' = 5'$ transition of the $D2$ line in cesium is at 852 nm, the cavity length should be adjustable over a range of at least 426 nm in order for the relevant transition to be always in resonance with the cavity modes. The translation of the cavity mirrors can be done by either the shear mode or the expansion mode of the piezoelectric plates. Shear mode refers to the relative displacement of the two electrodes in their own planes; expansion mode refers to the expansion of the piezo perpendicular to the direction of the electric field. Note that the excitation of the shear mode and the expansion mode require two different poling processes, so that only one of the modes is excited in each piezoelectric plate.

For shear mode piezoelectric plates,

$$Distance\ traveled = d_{15} \cdot Voltage \tag{2.1}$$

To obtain longer travel, we can apply a higher voltage up to the breakdown voltage of $\approx$ 1000 Vper mm. For Pz27 piezoelectric shear plate from Ferroperm Piezoceramics, d_{15} = 500pm/V, which implies a voltage of 852 V is required for a tunable cavity length of 426 nm.

For expansion mode piezoelectric plates,

$$Distance\ traveled = \frac{d_{31} \cdot Voltage \cdot Length}{Thickness} \tag{2.2}$$

For Pz27 piezoelectric expansion plate from Ferroperm Piezoceramics, d_{31} =

170pm/V. Since the separation between the base of the cavity mirrors is 2 mm, even at its breakdown voltage of 1 kV, we only have 340 nm for the tunable cavity length. One solution would be to align the cavity very carefully outside the chamber so that the relevant transition of the cesium atom is in resonance. This is difficult because differences in thermal expansions of various components can change the cavity length after it is pumped to ultra-high vacuum and baked. In addition, the observed displacement may be different from the predicted value. For instance, previous cavities in both lab 1 and lab 11 in our group traveled four times the expected distance [3], but cavities in the Chapman group at Georgia Tech traveled only one-third the expected distance [18]. Therefore, we also considered indirect mounting so that the cavity length is adjusted with a longer piece of piezo. Other possible approaches include using a piezo with a larger piezoelectric modulus d_{31} or with a higher breakdown voltage, but I have been as yet unable to find any that satisfy our vacuum criteria.

We have two ways to measure the tunable range of our designs. First, we can build a cavity and measure the resonant modes. Second, we can put a plane mirror on the mount and measure its range of travel with a Michelson's interferometer (Fig. 2.2). We chose the latter method for our tests, as the experimental setup is much simpler.

2.5 Designs of the mirror mount

I proposed three major designs for the mirror mount.

Design 1 Two cavity mirrors are glued directly onto an expansion-mode piezo plate (Fig. 2.3). This design originated at the Chapman group at Georgia Tech [18]. It is simple and is mechanically stable. Using this design, Cavity QED experiments at the Chapman group achieved a drift in cavity length smaller than 1 fm/s over 100 s passively when the mount was suspended by four Cu-Be springs. However, we would only have 340 nm for the tunable cavity length with this design. That implies that we would have to align the cavity very carefully outside the chamber. It was not a problem for the Chapman group because their piezoelectric modulus,

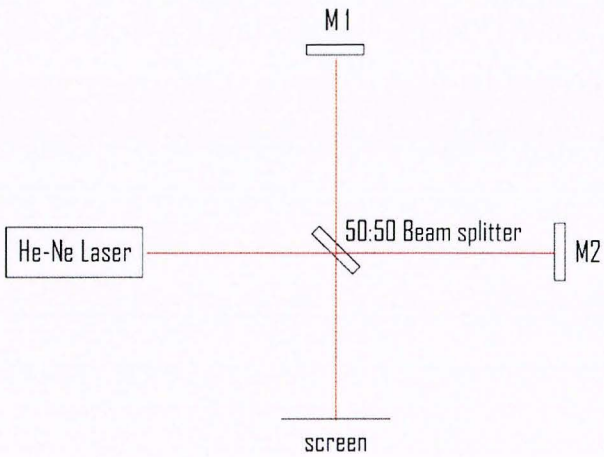

Figure 2.2: A simplified schematic of the experiment setup of the Michelson's interferometer. Plane mirror M1 is fixed while plane mirror M2 is mounted onto the piezo. By using a He-Ne laser, we are sensitive to displacements $\sim$ 300 nm.

$d_{31} = 225\text{pm/V}$, was 1.3 times larger than ours and their cavity was 2.5 times longer compared with our setup. Although our piezo has a smaller piezoelectric modulus, our piezo is bakeable to a higher temperature. The other disadvantage of this design is that it couples the adjustment of cavity length and the induction of birefringent splitting through mechanical stress. It is unclear whether the changes in birefringent splittings are significant when the cavity length is being adjusted. More practice at cavity alignment and measurements on birefringent splittings are needed if we plan to use this design.

Design 2. We cut slits of about 200 μm in width into a piece of metal (manufactured by a process called Electrical Discharge Machining), and these slits form a spring system (Fig. 2.4). The mirrors can be mounted on the two sides of the spring structure by glues or wires, although the use of glue might be more stable mechanically. The mount is made of aluminum because of both its low outgassing rate and elasticity. This design originated with Michael Chapman (a test mount that he built while he was a postdoc in the Kimble group) and the suggestions of Kevin Birnbaum. It has four advantages. First, using a linear model, the separation between the two

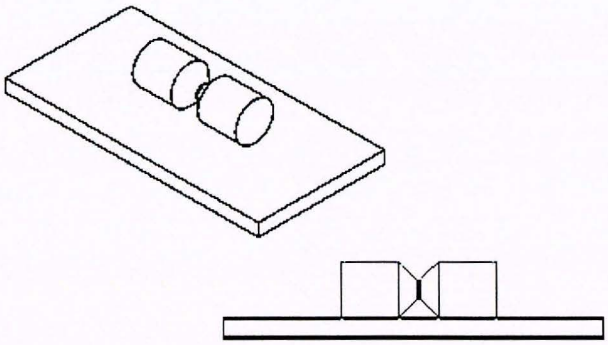

Figure 2.3: **Design 1**. Two cavity mirrors are glued directly onto an expansion mode piezo plate. This design is simple and is mechanically stable. When the mount was suspended by four Cu-Be springs, a drift in cavity length smaller than 1 fm/s over 100 s was achieved passively by the Chapman group at Georgia Tech [18]. However, this design only gives a tunable cavity length of 340 nm, compared with our goal of 426 nm.

mirrors is predicted to be adjustable over a range of 700 nm. Second, since both mirrors are affected by the same piece of piezo, so it is hoped vibration can be better controlled. Third, if the mirrors are held by wires, we can avoid using any glue, and hence, it is better for deployment in vacuum. Fourth, we might control the induction of birefringent splitting by applying mechanical stress with the wires, regardless of whether we mount the mirrors with only wires or both glue and wires. If we use only wires, we can, in principle, decouple the adjustment of cavity length and the induction of birefringent splittings through mechanical stress.

I tested a prototype of this mount with the Michelson's interferometer (Fig. 2.2). We observed a shift of a He-Ne laser fringe ($\lambda/2 = 316.5$nm) with only 25 V applied on the piezo. We later found that the angle between the mirror and the vertical changed by 7.2 arc seconds when a voltage of 25 V was applied on the piezo. The implication of a shift of a fringe was not clear, since the shift could be caused by a horizontal motion of the mirror, a misalignment of the two laser beams caused by a tilt of the mirror, or both. We originally thought the entire mount was bent as the piezo expanded. Nonetheless, this hypothesis was not supported by the fact that the tilt angle still changed by a similar amount even if the bottom of the mount was

entirely glued onto a block of aluminum. Since the changes in tilt angle were different on the two sides of the mount, it was suspected that the angular motion was due to nonuniform compression of aluminum. More tests are needed to confirm the causes of the angular motion.

Our tests indicated that this design has to be modified. As our cavity mirrors have a finesse $\sim 10^6$, a photon on average bounces back and forth a million times in the cavity before it is transmitted through the mirror. Given that the reflecting surfaces of the mirrors are 1 mm in diameter and that the cavity length is 40 μm, that implies the cavity mirrors cannot be tilted by more than half an arc second. Otherwise, the photon will "walk off" the cavity axis.

Two points should be noted in further modifications of this design. First, the loading process of the piezo onto the mount needs to be improved. In our prototype mount, we "snapped" the piezo into the mount and in the process, broke several pieces of piezo. Second, finite element analysis (FEA) should be used to model the motion and the resonant frequencies of the mount. Since the motion required is of the order of 100 nm, the mount can be adequately modeled as a linear system [28]. On one hand, in order to obtain longer travel, we need to lower the effective spring constant k in our design. On the other hand, resonant frequencies are proportional to $\sqrt{k}$, which means we would like to make the effective spring constant k larger. It is not obvious that there exists at least one solution. In addition, as the spring system becomes more complicated, FEA can help in predicting the angular motion of the cavity mirrors.

Design 3. The cavity mirrors are glued directly onto the shear mode and the expansion mode piezoelectric plates respectively. This design is a modification of the current cavity setup, which originated with former Kimble lab graduate student Theresa Lynn [3]. There are two differences between the new design and the current cavity. First, I have replaced the piezos in the current cavity by bakeable ones. Since the piezoelectric material used in the past cavity has a Curie temperature of only 290 °C, the past cavity could not be and was not baked. Second, I propose replacing one of the shear mode piezos in the current cavity by an expansion mode piezo. With only the shear mode piezo, the cavity length should be adjustable over a range of at least

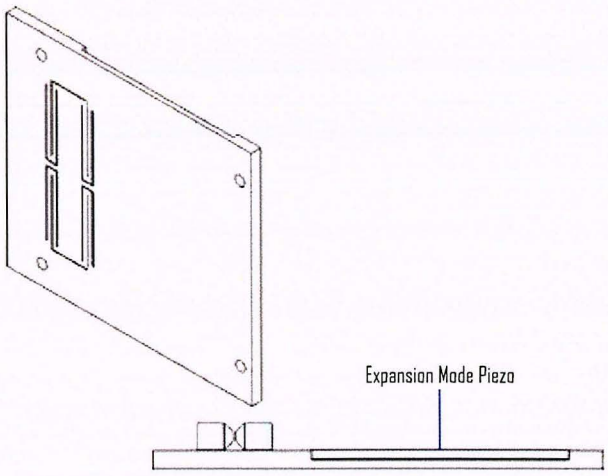

Figure 2.4: **Design 2**. The slits are about 200 μm wide and they form a spring system. The mirrors can be mounted on the two sides of the spring structure by glues or wires. This design has four advantages: larger tunable range, improved mechanical stability, better vacuum compatibility and plausible control over birefringent splittings compared to past cavities. However, tests on a prototype indicated that this design has to be modified, since the angular motion of the mirrors while tuning the cavity length was too large and light can "walk off" the cavity axis.

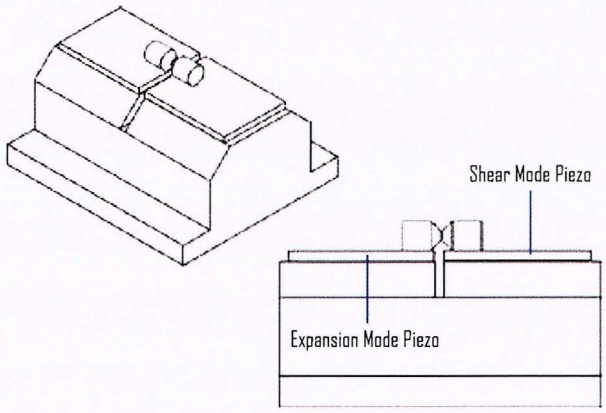

Figure 2.5: **Design 3**. The cavity mirrors are glued directly onto the shear mode and the expansion mode piezoelectric plates respectively. This design is a modification of the current cavity, and there are two differences between the new design and the current cavity [29]. First, the new cavity is bakeable. Second, one of the shear mode piezo in the current cavity is replaced by an expansion mode piezo. With only the shear mode piezo, the cavity length is supposed to be adjustable over a range of at least 426 nm. The expansion mode piezo might be used to induce birefringent splittings through mechanical stress. This design has the advantage that the adjustment of cavity length and the control of birefringent splittings are decoupled. Since design 3 is only a slight modification of the cavity used in current experiments, we are most likely to use it for cavity constructions in the near future.

426 nm. The expansion mode piezo might be used to induce birefringent splittings through mechanical stress. This design has the advantage that the adjustment of cavity length and the control of birefringent splittings are decoupled. However, more tests and modelings are needed to determine the effects on birefringent splittings when the cavity mirrors are stressed in the axial direction.

Since design 3 is only a slight modification of the cavity used in current experiments, we are most likely to use it for cavity constructions in the near future. In Chapter 6, I will discuss preliminary measurements of birefringent splitting induced by a variation of this design.

Chapter 3

Construction of the Cavity

This Chapter summarizes the procedures that graduate student Dal Wilson and I followed for cavity construction. Our starting points were Kevin Birnbaum's unpublished "Making a cavity"notes [30], in addition to Christina Hood's thesis [29], but we have added our own modifications to these established procedures.

Our eventual goal is to build a single-sided cavity (Section 1.6), with bakeable piezoelectric transducer and higher quality mirrors. The new mirrors are custom-made by Research, Electro-Optics, Inc. (Boulder, CO), which in mid-nineties also manufactured the cavity mirrors used in current Kimble lab experiments. In the future, we may use better mirrors from an emerging company, Advanced Thin Films (Longmont, CO).

3.1 Building my first cavity

Making a high finesse cavity is a nontrivial task. According to Kevin Birnbaum, a former Kimble lab graduate student, it takes ten days to construct a vacuum-compatible cavity. Noting the great difficulties in assembling modified cavities encountered by my fellow SURF student Toby Burrows over the summer [31], Dal Wilson and I decided to build a cavity by following Kevin's procedures exactly as a practice exercise before adding in any modifications. Below is a summary of the procedures I used for cavity construction.

1. **Baking the mounts.** Clean a copper mount and two V-blocks, and then bake

them in a vacuum oven at 200 °C for 48 hours.

2. **Cutting the piezo.** Scratch two arrows pointing toward the marked edge of a piece of EBL 3 shear-mode PZT from Staveley Sensors Inc. (East Hartford, CT) with a Thorlabs fiber scribe (Newton, NJ). Break off two $1/2'' \times 1/4''$ pieces of piezo by first scoring it deeply with the Thorlabs fiber scribe and then pressing the scored edge against a straight edge.

3. **Cleaning the piezos.** Ultrasound both piezos in methanol for 2 – 3 minutes and then rinse them with isopropyl.

4. **Attaching the piezo.** Attach the piezo to the copper mount by first applying a uniform thin film of Dynaloy 325 conductive epoxy from Kurt J. Lesker Company (Pittsburgh, PA) to the piezos, sandwiching the unit between two clean microscope slides and then compressing the unit in a vise. Check for short circuits between the top electrodes of the piezos and the copper mount and clean off any excessive epoxy with acetone if necessary.

5. **Attaching the ground wire.** Scrape off some insulation from both ends of the 36 HML kapton-coated wires from MWS Wire Industries (Westlake Village, CA) with a razor blade. Clean the wires by wiping them with methanol. Since it is difficult to heat up the copper mount, attach the ground wire to the copper mount with the Dynaloy 325 conductive epoxy instead of soldering. Allow the epoxy to cure for 24 hours.

6. **Connecting the electrodes.** Connect the electrodes by soldering the kapton-coated wires to the piezo using the 62% Sn/36% Pb/2% Ag solder. Make sure the temperature of the soldering iron is lower than 200 °C, and finish soldering within 30 s as the silver electrodes are soluble in the solder. Remove the soldering flux by rinsing with water.

7. **Baking the unit.** Bake the unit in a vacuum oven at 120 °C for 24 hours.

8. **Attaching the V-block.** Glue one V-block to one of the piezos with Torr-Seal from Varian, Inc. (Palo Alto, CA). Use a thicker layer of glue as necessary to allow more room to align the second V-block. Allow the epoxy to cure for 24 hours.

9. **Setting up the Cavity Testing Breadboard.** Clean off the area around the cavity testing breadboard (Fig. 3.1) and turn on the blowers for the clean hood. Make sure the filters of the blowers are clean. Carry on all the following procedures in the clean hood.

10. **Attaching the entrance mirror.** Clean the cavity mirrors under the microscope, as described in Christina Hood's thesis [29]. Attach the cavity entrance mirror to the V-block that is already attached to the copper mount, which is sitting on a 3-dimensional translation stage NF15AP25 from Thorlabs, Inc. (Newton, NJ), and the cavity exit mirror to the other V-block, which is held by a jig in the Lees mount (Fig. 3.2), using the EP30LTEND epoxy from Master Bond Inc. (Hackensack, NJ). Allow the epoxy to cure for 48 hours.

11. **Rough alignment with the HeNe.** The step is necessary because the power transmission of our cavity mirrors is only a few or tens of ppm near 852 nm, and we will not be able to see the beam using an infrared (IR) fluorescent card or a IR sensitive camera during alignments. In contrast, the mirrors are not highly reflective at the HeNe wavelength of 635 nm, so this wavelength can be seen easily. First, align the optics visually. The alignment will be easier if the angles of incidence are 45 ° for the two mirrors closest to the cavity. Second, align the incoming beam such that it coincides with its retroreflection from the cavity entrance mirror. Note that there are two retroreflection spots from the cavity entrance mirror; the large spot corresponds to reflection from the mirror surface, and the smaller one corresponds to the reflection from the mirror substrate. Since there is slight wedge at the back of the mirror substrate, do not attempt to align the smaller retroreflection spot with the incoming beam. It is important to note that Christina Hood's thesis suggested otherwise [29], but it does not

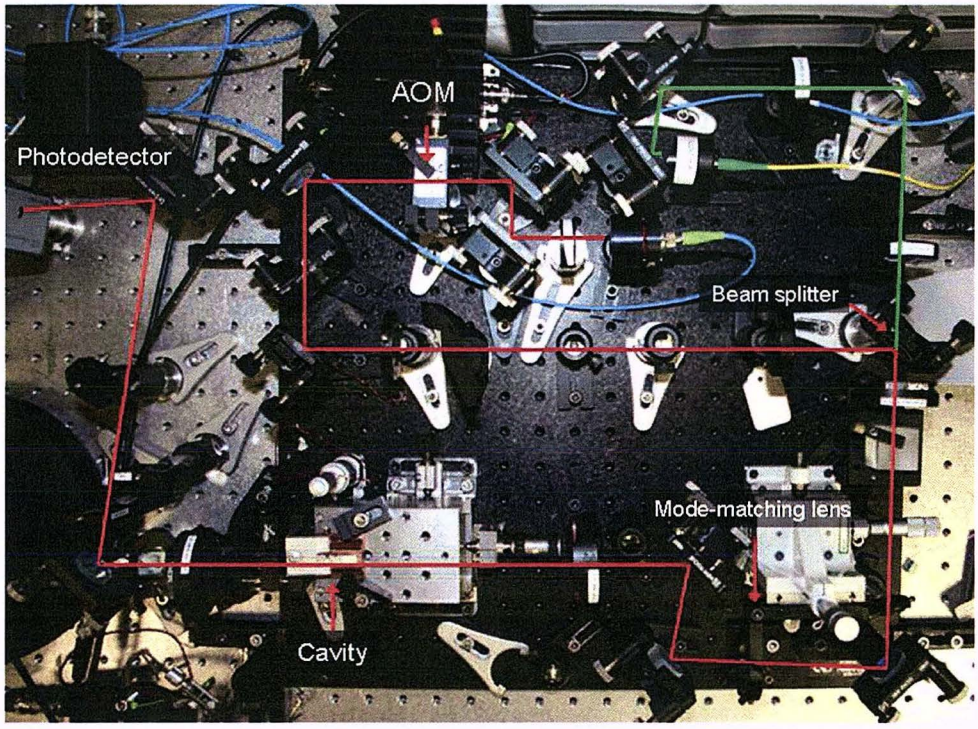

Figure 3.1: Cavity testing breadboard: The HeNe and the 852 nm beam paths are marked as green and red respectively. The 852 nm beam passes through an acousto-optic modulator (AOM) and overlaps with the HeNe beam on a beamsplitter before entering the cavity. By switching on/off the radio-frequency (RF) signal to the AOM, we can switch on/off the 852 nm beam in 50 ns and perform ring-down measurement (Chapter 4). The various lenses, mirrors, waveplates and polarizing beamsplitter cubes are used to adjust the sizes, positions and polarizations of our beams. I built a new cavity testing breadboard in the spring of 2005.

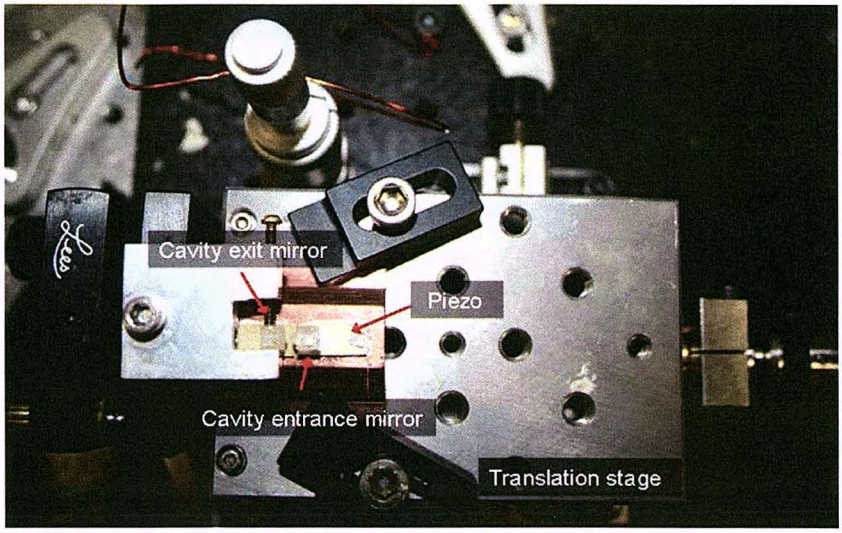

Figure 3.2: The cavity entrance mirror is attached via a V-block to the copper mount, which is sitting on a 3-dimensional translation stage; the cavity exit mirror to the other V-block, which is held by a jig in the Lees mount.

apply to our new cavity mirrors. Third, adjust the cavity exit mirror such that the reflections from both cavity mirrors coincide with the incoming beam. At a much greater distance than the radius of curvature (5 or 10 cm) of the exit mirror, the smaller reflection spots correspond to reflections from the mirror substrates, and they are not important. Check if the beam is going straight through the hole on the jig holding the cavity exit mirror. If it is not the case, repeat the above step as necessary. Fourth, insert the "mode-matching" lens (Fig. 3.3), and repeat the above alignment procedures only by translating the lens perpendicular to the laser beams. The mode-matching lens adjusts the spot size so that the 852 nm light can couple to the cavity efficiently. We did not include the lens initially because the alignment is very sensitive to its position.

12. **Alignment with the 852 nm beam.** First, it is important to make sure that the power of the beam is less than 10 μW, as higher power can damage the cavity mirrors. Second, align the 852 nm beam with the HeNe beam by adjusting only the 852 nm. Third, set up the cavity output on an infrared-sensitive camera.

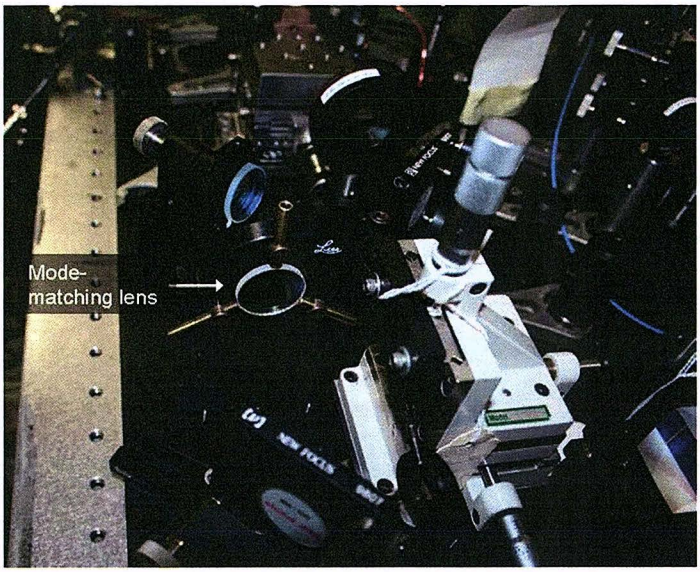

Figure 3.3: The mode-matching lens on the translation stage adjusts the spot size so that the 852 nm light can couple to the cavity efficiently.

While looking at the camera, adjust the cavity length by tuning the piezoelectric voltage until a resonant mode is observed (Fig. 3.4, 3.5, 3.6). The voltage for the piezoelectric transducer underneath the one glued mirror is provided by a 300 V battery with a modulation from a function generator, using the wires we attached in steps 5 and 6. The other mirror, held in the Lees mount jig, remain fixed. If no resonant mode can be observed, repeat the above alignment procedures. If no resonant mode is observed after several iterations, remove the mirrors from the V-blocks with a razor blade and check for dust particles under the microscope. Finally, optimize the TEM_{00} mode by adjusting the position of the mode-matching lens (located on a translation stage), while looking at the cavity transmission with a photodiode.

13. **Measuring the finesse.** Determine the finesse of the cavity through ring-down measurement (Chapter 4).

14. **Adjusting the cavity length.** Adjust the position of the entrance mirror

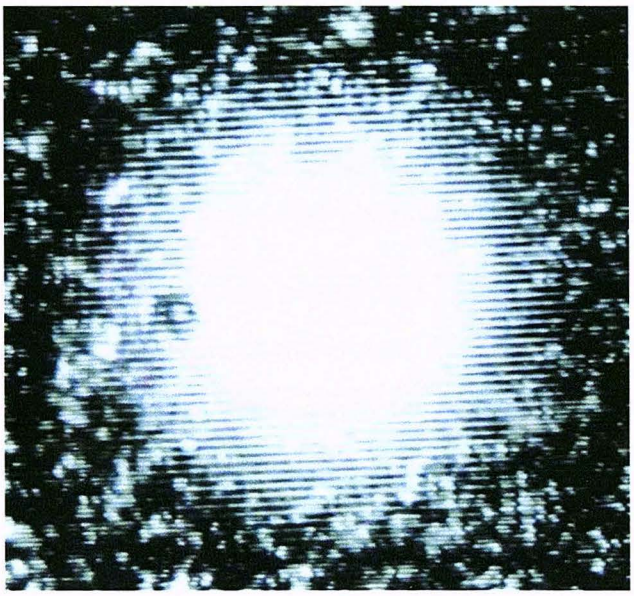

Figure 3.4: Cavity transverse mode: TEM 00. This picture was taken with an IR camera as the cavity length was tuned through an adjustment of the piezo voltage.

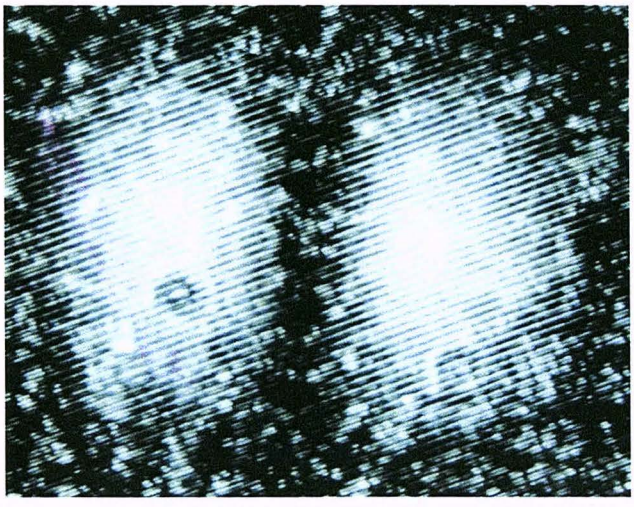

Figure 3.5: Cavity transverse mode: TEM 01

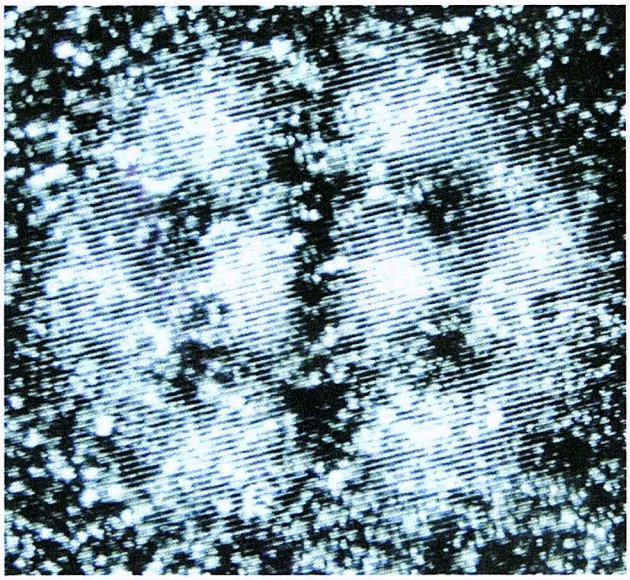

Figure 3.6: Cavity transverse mode: High Order

along the cavity axis with the translation stage while monitoring the cavity length with a Ti:Sapph laser, as discussed in Chapter 5.

15. **Attaching the cavity exit mirror.** Note the reading on the translation stage before lowering the mirror mount. Once there is sufficient space to bring in an applicator, apply Torr-Seal to the bottom of the V-block that holds the cavity exit mirror and then raise the mirror mount to its previous height. Monitor the cavity length for at least two hours as the glue sets, adjusting it if necessary.

3.2 Summary of modifications to the original procedures

1. We now clean our cavity mirrors with cotton swabs HUBY-340 from Sanyo, Co. (Tokyo, Japan) instead of folded lens paper as recommended by Christina Hood [29]. We did not notice any difference in term of cleaning quality, but it was more efficient to use cotton swabs.

2. Due to the slight wedge at the back of the mirror substrate, we now align the retroreflection from the mirror surfaces but not those from the mirror substrates with the incoming beam, which is different from the procedures described in Christina Hood's thesis [29].

3. We now search for the resonant modes with an infrared sensitive camera instead of using a photodiode signal on an oscilloscope. There are two advantages for using the camera. First, it is a lot easier to pick out weaker resonant modes with the camera because the Charge-Coupled Device (CCD) integrates the signal for a long time period and the light is harder to miss due to the larger detector area. Second, we can observe the structure of the TEM_{00} mode directly and compare it visually to the other higher-order modes (Fig. 3.4, 3.5, 3.6). With the photodiode, we can only infer the observation of the TEM_{00} mode by noting it is the first of the set of resonant modes, which appear as peaks in transmission as the piezo voltage is scanned. This can be tricky when the first mode is weak.

4. We now recommend checking the cavity mirrors for dust particles under the microscope if no resonant mode is observed after several iterations of the alignment process.

3.3 Lessons learned from my first cavity construction

Due to various technical difficulties, it took much longer than we had expected to build the first cavity. Our major obstacle to the observation of cavity resonances was dust particles deposited on the cavity mirrors. Although we cleaned our cavity mirrors under the microscope right before cavity construction and built the cavity inside the clean hood with the blowers on, there were enough dust particles deposited on the mirror surfaces to prevent cavity resonance if the two mirrors were about a few mm apart for a couple of hours. It was a problem for us initially because it took us at least half a day to do the rough alignment. After building several cavities, we can

now align a cavity within three hours. It took us a few months to realize that dust particles instead of alignment or mechanically stability were the heart of the problem and to discover we had a dirty filter in the blowers. After replacing the filter, keeping the mirrors free of dust for the duration of cavity construction is no longer a problem.

3.4 Construction of modified cavities

Upon the completion of the first cavity, more cavities, each with slight modifications from the original design, were built as steps toward our next-generation cavity.

Hoping to improve passive mechanical stability, Dal and I attempted to build a cavity without V-blocks using a new jig I designed, but the mirror could be easily cracked by the jig during cavity construction. Moreover, the residual stress in the mirrors resulting from direct contact with the jig can result in more birefringent splitting. Therefore, we do not recommend building a cavity without V-blocks unless a new method is developed.

We also built cavities with the use of H27DUHV conductive epoxy from Caburn MDC (West Sussex, U.K.), which is supposed to improve the outgassing rate of our system, in place of the Dynaloy 325 epoxy and Torr-Seal. Since the new epoxy cures only if heated above 150 °C for an hour, we heated our cavity by blowing it with hot nitrogen for two hours (Fig. 3.7). We did not bake it in the oven because we needed to monitor the cavity length with the lasers as the epoxy set; we did not use a heat gun because dust particles can be carried to the mirrors.

We also built a single-sided cavity (Section 1.6). The power transmissions are 15 ppm for the transmissive mirror and 0.2–0.5 ppm for the non-transmissive. Scattering and absorption lossed for these "practice" mirrors were 3–4 ppm but will be lower in the final cavity mirrors. During cavity alignments, the more transmissive mirror was the exit mirror so that we could detect the resonant light on the photodiode. We did not have any major difficulties in building the single-sided cavity except that the resonance was very narrow, but this is generally true for any high finesse cavity. We only have to tune the cavity length more carefully when searching for resonances.

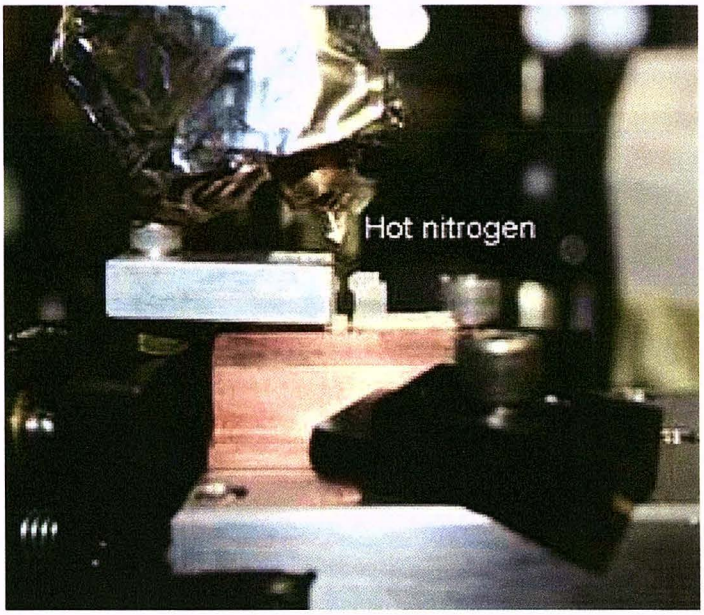

Figure 3.7: We heated our cavity with hot nitrogen in order for the H27DUHV epoxy to cure. Depending on the distance from the tip of the copper tube and the angle, the temperature near the tip ranged from approximately 150 °C to 200 °C.

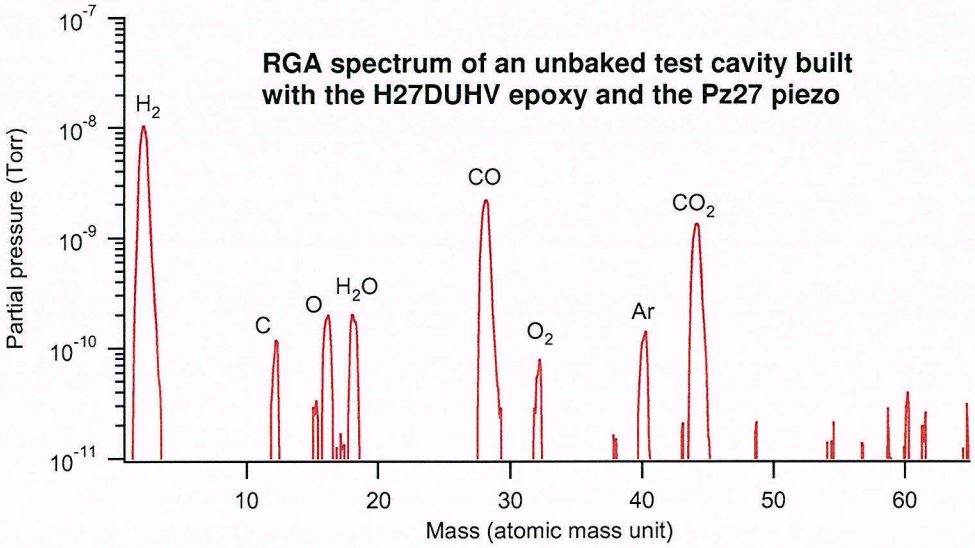

Figure 3.8: The RGA spectrum of a test cavity built with the H27DUHV epoxy and Ferroperm Pz27 piezo, after pumping down for a week.

In order to test the vacuum compatibility of the new cavity materials, we built another cavity using the H27DUHV epoxy and Pz27 from Ferroperm Piezoceramics (Kvistgaard, Denmark) in place of Torr-Seal and Staveley EBL 3 PZT. We put this cavity inside a vacuum chamber, baked at 250 °C for three days and pumped down the chamber for a week, while monitoring the partial pressure with a Residual Gas Analyzer (RGA). Unfortunately, it was discovered that the RGA was short-circuited to the wall of the chamber throughout the process. We opened the chamber for a few hours, fixed the RGA and closed the chamber. We then pumped down the chamber for a week, but we did not bake the chamber again. The RGA spectrum (Fig. 3.8) shows that the partial pressures are relatively low for a chamber that was not baked seriously. However, we need to seriously bake the chamber and measure the pressure again before we can conclude that the new materials are indeed better for the vacuum.

Additional cavities were then built with mechanical stress actively induced on the cavity mirrors with piezoelectrics. These results will be discussed in Chapter 6.

Chapter 4

Measurements of Finesse

This Chapter discusses the measurement of the cavity finesse and presents the results on our cavity. A more detail discussion of the measurements of finesse can be found in ref. [10].

4.1 Cavity finesse

A Fabry-Perot cavity is characterized by its finesse

$$F = \frac{\pi}{T_1 + T_2 + A_1 + A_2} = \frac{\Delta\nu_{FSR}}{\Delta\nu_{fwhm}} \tag{4.1}$$

where T_1, T_2 (A_1, A_2) are the power transmissions (power losses due to scattering and absorption) of mirror 1 and mirror 2 respectively, $\Delta\nu_{FSR}$ is the free spectral range and $\Delta\nu_{fwhm}$ is the cavity linewidth [9]. Note that Eq. 1.1 only applies to ideal high-finesse cavities made of mirrors of high reflectivity.

Eq. 4.1 suggests two ways to measure the finesse, namely by measuring $\Delta\nu_{FSR}$ and $\Delta\nu_{fwhm}$ or by measuring the total cavity loss per mirror. Since it is more time consuming to calibrate $\Delta\nu_{fwhm}$ by putting on frequency sidebands with an electro-optic modulator (EOM), we chose the latter method.

We infer the cavity loss by measuring the cavity decay time constant τ. For round-trip time $\Delta t << \tau$, the transmitted power decays exponentially with τ given by

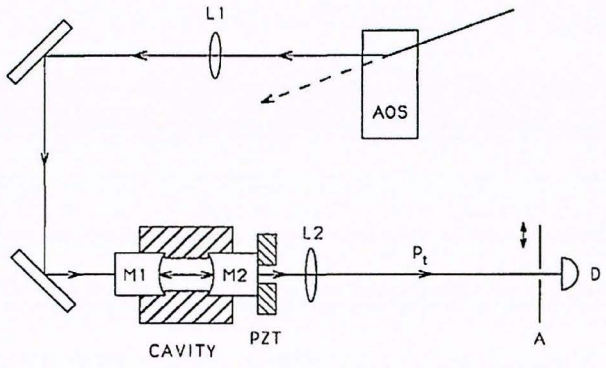

Figure 4.1: A schematic diagram of the experimental setup for the ring-down measurement [10].

$$\tau = \frac{\Delta t}{(T_1 + T_2 + A_1 + A_2)} \tag{4.2}$$

where the total loss $L = T_1 + T_2 + A_1 + A_2$, and

$$F = \frac{2\pi}{(T_1 + T_2 + A_1 + A_2)} = \frac{2\pi\tau}{\Delta t} = \frac{\pi\tau c}{d} \tag{4.3}$$

where d is the cavity length and c is the speed of light in air.

4.2 Ring-down measurement

Experimentally, we measured the cavity decay time constant τ using an acousto-optic switch (AOS, Fig. 4.2) and a fast photodetector (Fig. 4.1) and the cavity length with a calibrated microscope (Fig. 5.1). Note that we measure the finesse before the exit mirror is glued down (see Chapter 3) and when the cavity is about a millimeter long. We slowly scanned the cavity length by tuning the piezo transducer voltage until the cavity was on resonance, and at that time the cavity transmission signal triggered the AOS to block the incident beam. The cavity transmission signal was recorded with a digital oscilloscope, and τ was determined by fitting the decay portion of the transmission signal to $I_0 e^{-\frac{t}{\tau}}$ (Fig. 4.3).

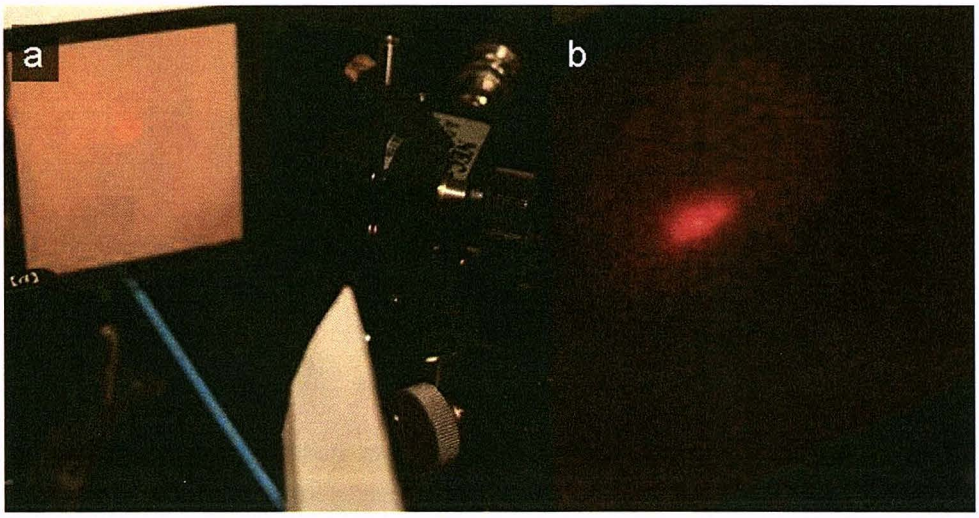

Figure 4.2: a) The 852 nm beam is passing through the radio-frequency (RF) signal driven acousto-optic modulator (AOM). The picture is taken with a help of an infrared fluorescent card. In the presence of the RF signal, the AOM acts as a diffraction gating, and therefore splits a single beam into two (or more) orders. We use an iris to block only the 0th order but not the 1st order beam so that our beam can be switched on/off by the RF signal. b) A close-up picture of the 0th and 1st order beams emerging from the AOM.

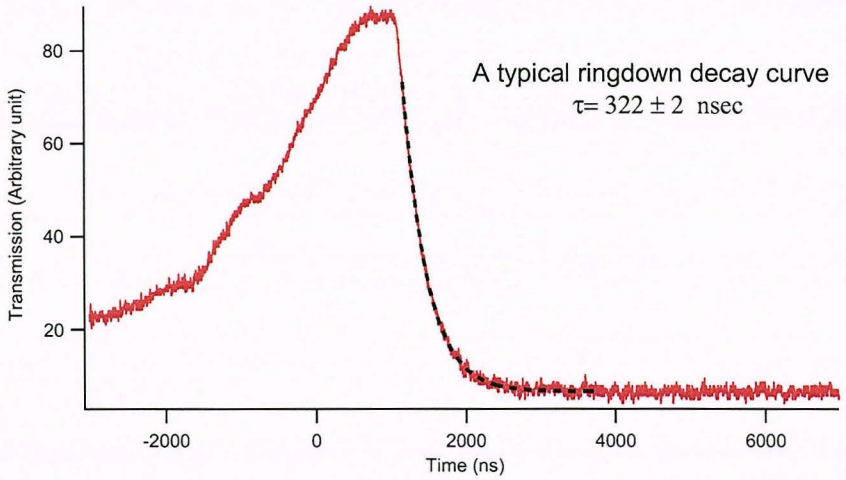

Figure 4.3: A typical ring-down measurement datum. The part of the transmission signal marked by the dashed curve is fitted to $I_0 e^{-\frac{t}{\tau}}$ in order to determine the decay time constant τ.

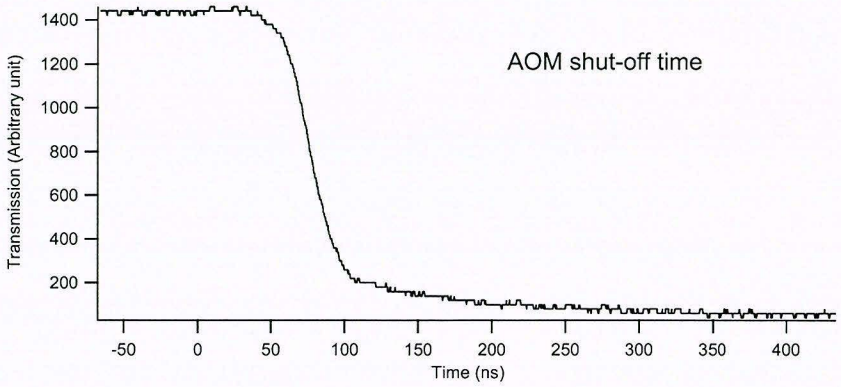

Figure 4.4: By terminating the radio-frequency signal to the acousto-optic modulator, the AMO shuts off the beam within 50 ns.

We repeated the ring-down measurement of our cavity eleven times, and the average time constant τ was (322.6 ± 4.3) ns. Since the fitted value of τ is much greater than the AMO shut-off time of 50 ns (Fig. 4.4), it was justified to fit our ring-down signal to a simple exponential, ignoring the decay during the shutoff of the AMO. The cavity length was measured to be (0.8 ± 0.1) mm. Therefore, the measured value of the cavity finesse $F = (3.8 \pm 0.5) \times 10^5$.

For our cavity mirrors, the power transmissions (T_1, T_2) and the power losses (A_1, A_2) are $T_1 = 16$ ppm, $T_2 = 0.2$–0.5 ppm and $A_1 = A_2 = 2$–4 ppm. Eq. 4.3 gives $F = (2.8 \pm 0.3) \times 10^5$, which agrees with our measured value (1.7σ).

Note that the time constant of the ring-down measurement decreases as we shrink the cavity length. With a AMO shut-off time of 50 nm, the minimum cavity length for which we can measure the finesse confidently using the above method is about 1 mm. As the finesse is alignment sensitive, we would like to measure the finesse at the final cavity length, which will be measured by determining Δ_{FWHM} with an EOM calibration and Δ_{FSR} from the cavity length measurement, as described in Chapter 5.

Chapter 5

Measurements of Cavity Length

This chapter describes the method I used to control and measure the cavity length in test cavities.

5.1 Choosing a specific cavity length

There are three major criteria in choosing a cavity length. First, the cavity length must be small. For a single photon interacting with an atom inside a cavity, the rate of coherent evolution of the system is given by

$$\hbar g_0 = |\vec{\mu}| \sqrt{\frac{\hbar\omega}{2\epsilon_0 V_m}} \tag{5.1}$$

where $\vec{\mu}$ is the atomic dipole, ω is the frequency of the photon and V_m is the mode volume of the cavity [3]. Given the cavity field decay rate κ and the atomic spontaneous emission rate γ, we must minimize the mode volume V_m in order to achieve strong coupling $g_0 >> (\kappa, \gamma)$. For the geometry of our mirrors, we need a cavity length of the order of tens of μm.

Second, the cavity length must be long enough to allow side-beam access. Our atoms acquire enough kinetic energy to escape the trapping potential of the FORT as they drop through a height of a few millimeters from the MOT to enter the cavity [29]. In order to load atoms more efficiently, in our new cavity we will employ a side beam cooling scheme, which involves bringing in four blue-detuned counter-propagating beams (the lattice beams) from the sides, as in current Kimble lab experiments [32].

These beams can also provide cooling while the atom is trapped in order to increase the trapping time.

For a Gaussian beam, the beam waist $w(r)$ at a distance r from the point of minimum beam waist is given by

$$w(r) = z \cdot \sqrt{1 + (\frac{r \cdot \lambda}{\pi \cdot z^2})^2} \tag{5.2}$$

where z is the minimum beam waist and λ is the wavelength of the beam [9]. Given that the lattice beams are focused at the center of our cavity, the beam waists at the edge of our cavity $w(r = 0.5 \text{ mm})$ achieve their minima for $z = 11.6$ μm. Therefore, the cavity length must be larger than 32.9 μm, which is the waist of our lattice beams at the edge of our cavity ($w(r = 0.5 \text{ mm})$).

Third, our cavity must be simultaneously resonant at 852.356 nm and near 935 nm. The 852.356 nm corresponds to the $6S_{1/2}, F = 4 \rightarrow 6P_{3/2}, F' = 5'$ transition of the $D2$ line in Cs, which is the transition between the two levels of our primary interest in a Cs atom; the 935 nm is known as the "magic wavelength" for the FORT, which is important to state-insensitive trapping of single Cs atom. In the two-level model of a Cs atom, the positive ac-Stark shift of the excited electronic states in the presence of a red-detuned FORT beam is comparable in magnitude to the negative shift of the ground state. As a result, the detuning between the atom and cavity resonances becomes spatially dependent. However, near the magic wavelength, the sums of ac-Stark shifts from all allowed optical transitions for the ground $6S_{1/2}$ and excited $P_{3/2}$ states are both negative and are comparable in magnitude, if the specific multilevel structure of Cs is taken into consideration. Therefore, a FORT near 935 nm can provide a trapping potential to a Cs atom, regardless of whether it is in the $6S_{1/2}$ or the $P_{3/2}$ states [13]. Since the finesse of the cavity is much higher at 852 nm ($F \sim 10^6$) than at 935 nm ($F \approx 2000$), the cavity length must be closer to resonances at 852 nm than at 935 nm.

Taking all three factors above into consideration (Table 5.1), we chose our cavity length L to be 88 half-wavelengths of 852.356 nm (i.e. $L \approx 37.5\mu$m).

$N_{\lambda/2}$ for 852.356 nm	$N_{\lambda/2}$ for 935 nm	Length in μm
22	20.1	9.4
77	70.2	32.8
88	80.2	37.5
99	90.2	42.2

Table 5.1: Short cavity lengths at which the cavity is simultaneously resonant at 852.356 nm and near 935 nm. $N_{\lambda/2}$ denotes number of half-wavelengths.

5.2 Cavity length measurement

Given that the length of our cavities is tunable over a range of $\sim$ 500 nm, we must be able to specify the cavity length within this tunable range when the cavities are built. Specifically, we measure the cavity length while the cavity exit mirror is held in the Lees mount jig and the other mirror is already fixed to the copper mount on the translation stage (Chapter 3). Once both cavity mirrors are glued to the piezoelectric transducers, we can tune the cavity into resonance with the predetermined $N_{\lambda/2}$ for 852 nm light only using these transducers, where $N_{\lambda/2}$ denotes the number of half-wavelengths. In practice, we aim at specifying the cavity length within 250 nm during cavity construction. Since our tunable range is limited, we have to distinguish between a resonance at the specified $N_{\lambda/2}$ and a resonance at $N_{\lambda/2} \pm 1$.

By measuring the frequency spacing between consecutive longitudinal modes (i.e. free spectral range ν_{FSR}), we can determine the cavity length L up to the order of $N_{\lambda/2}$. Operationally, we first tuned the cavity length to $\sim$ 40 μm by adjusting the position of the cavity entrance mirror with the translation stage while monitoring the cavity length with a calibrated microscope (Fig. 5.1). Then we tuned the cavity into resonance at 852 nm with the piezoelectric transducer. While holding the cavity in resonance with 852 nm light from a diode laser, we detuned the wavelength of a adjustable Ti:Sapph laser from 852 nm to its neighboring cavity resonant wavelength. We measured the wavelength of the Ti:Sapph laser with a Burleigh wavemeter from EXFO Electro-Optical Engineering Inc. (Quebec, Canada), which has a precision of 1 pm. We calculated the free spectral range of the cavity and checked if $N_{\lambda/2}$ was at the desired value (Table 5.2). We adjusted the position of the cavity entrance mirror

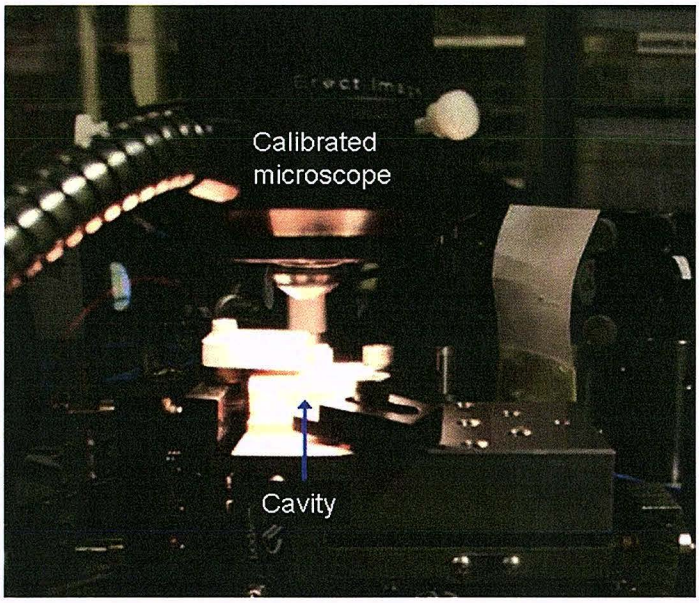

Figure 5.1: Using a calibrated microscope, we tuned the cavity length to ~ 40 μm by adjusting the position of the cavity entrance mirror with the translation stage.

using the translation stage and repeated the measurement of the free spectral range until the predetermined value of $N_{\lambda/2}$ was obtained. After we glued down the cavity exit mirror, we continued monitoring the cavity length using the above method for more than two hours as the glue was curing. After the glue was completely cured, we repeated the free spectral range measurement to check the cavity length.

In Febrary 2006, Dal and I built a cavity with $N_{\lambda/2} = 98$ for 852 nm. We were intending to build a cavity with $N_{\lambda/2} = 88$ or 99 for 852 nm, but we were unable to because the micrometer on the translation stage had a serious backlash in the ranges of interest. Before we glued down the mirror, our cavity was resonant at 843.704 nm, 852.356 nm, 861.141 nm and 870.123 nm. We did not search for the resonance near 835 nm because the Ti:Sapph laser was not very stable around that wavelength. We suspected that the slight discrepancies between the measured neighboring resonant wavelengths and those values in Table 5.2 were due to small amplitude vibration of the cavity mirrors. Nonetheless, we were confident that $N_{\lambda/2} = 98$ for 852 nm was

$N_{\lambda/2}$ for 852.356 nm	Neighboring resonant wavelength in nm
86	832.984, 842.559, 862.384, 872.650
87	833.202, 842.670, 862.267, 872.411
88	833.415, 842.779, 862.153, 872.178
89	833.623, 842.885, 862.042, 871.950
90	833.827, 842.989, 861.933, 871.728
97	835.137, 843.658, 861.235, 870.300
98	835.309, 843.746, 861.143, 870.113
99	835.478, 843.832, 861.054, 869.930
100	835.643, 843.917, 860.966, 869.751
101	835.805, 844.000, 860.880, 869.575

Table 5.2: Neighboring resonant wavelengths for $N_{\lambda/2}$ for 852.356 nm, where $N_{\lambda/2}$ denotes number of half-wavelengths. The table shows that a resolution of 0.1 nm for the measurement of the neighboring resonant wavelengths is sufficient to distinguish $N_{\lambda/2} = 88$ or 99 for 852.356 nm from $N_{\lambda/2} \pm 1$.

obtained with our cavity. We found that the cavity length drifted less than 400 nm and the cavity could still be tuned to resonate at $N_{\lambda/2} = 98$ for 852 nm after the glue was cured overnight. Once we replace the micrometer on the translation stage, we should be able to build a cavity with $N_{\lambda/2} = 88$ for 852 nm.

Chapter 6

Birefringent Cavity

This chapter describes a simple model of cavity birefringence I developed and the experimental tests we carried out on birefringence. Note that this chapter deals with symmetric cavities, as they are well understood.

6.1 Cavity birefringence

When beams of orthogonal polarizations are reflected by a mirror, a relative phase shift is often introduced between the two polarizations. The phase shift is caused by differences in the optical length due to variations in the index of refraction in response to nonuniform stress in the mirror. This effect is known as birefringent splitting. In our cavity system, the nonuniform stress in the mirrors is believed to be induced by glue, which holds the mirrors to the mount [3].

Birefringent splitting can present complications to our experiments because the cavity now supports two orthogonal, nondegenerate modes. For instance, a birefringent cavity does not support certain schemes of adiabatic passage generation of single photons [33] in which the final state of the system is the maximally entangled state between the photon and the atom inside the cavity [25].

In other occasions, birefringent splitting can be exploited to our advantages. For example, there is a adiabatic passage scheme [33] in which we can utilize cavity birefringence to enhance the generation of single photons with certain polarization [25].

Therefore, it would be very helpful to our experiments if we could actively control cavity birefringence, either to eliminate it completely or to set it to a convenient value.

6.2 A simple of model of cavity birefringence

I adopted the model of a cavity based on the transfer-matrix formalism from Ref. [34] and incorporated birefringent properties in my model. Since our cavity length is much shorter than the Rayleigh range, I used the plane-wave approximation.

The coating on our mirrors is a 37-layer stack of alternating tantalum pentoxide (Ta_2O_5) and fused silica (SiO_2) layers. At the center wavelength $\lambda_C = 852$nm, the refractive indices are $n_H = 2.0411$ and $n_L = 1.455$ for Ta_2O_5 and SiO_2 respectively. These indices vary within 0.1% in the region of interest ($800 - 900$nm), and hence, I assumed they are constant in my model.

In the transfer-matrix formalism, each layer j is represented by

$$M_j = \begin{bmatrix} \cos(kh_j) & [i\sin(kh_j)]/Y_j \\ iY_j \sin(kh_j) & \cos(kh_j) \end{bmatrix}$$

for normal incidence, and the input and output electric field E and magnetic field H are given by

$$\begin{bmatrix} E_{out} \\ H_{out} \end{bmatrix} = [M] \begin{bmatrix} E_{in} \\ H_{in} \end{bmatrix} \tag{6.1}$$

where $k = 2\pi/\lambda$ is the wave vector of the incident light in vacuum, $h_j = n_j \cdot$ *layer thickness* and $Y_j = \sqrt{\epsilon_0/\mu_0} n_j$, with ϵ_0 and μ_0 the electric and magnetic constants in SI units [34].

In this formalism, each mirror is represented by $M_m = (M_{Ta_2O_5} M_{SiO_2})^{18} M_{Ta_2O_5}$, and the cavity is represented by $M_c = M_m M_g M_m$, where M_g is the transfer matrix for the vacuum gap between the mirrors. The cavity transmission T is given by

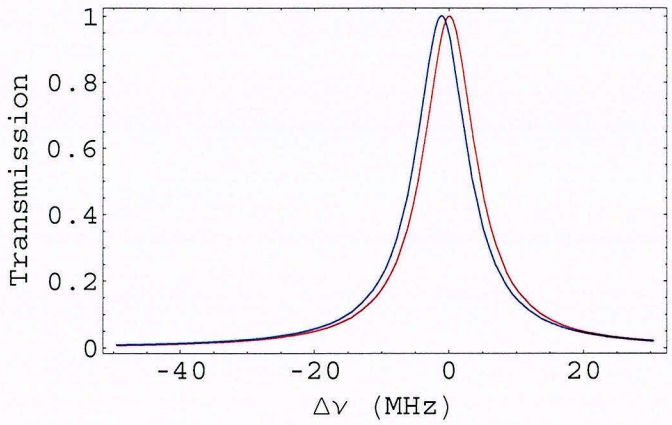

Figure 6.1: Transmission profiles with (blue) and without (red) a change in the refractive index $\Delta n = 3 \times 10^{-7}$. $\Delta\nu$ is the laser detuning from the cavity resonance at 852 nm. The linewidth (FWHM) of the transmission profile is 9.3 MHz and the birefringent splitting is 1.1 MHz, which corresponds to a fractional splitting of 0.1. These calculated values are of the same order of magnitude with typically observed values in our cavities used in past experiments [3, 32].

$$T = \left| \frac{2Y_s}{(Y_s M_{11} + Y_s^2 M_{12} + M_{21} + Y_s M_{22})} \right|^2 \tag{6.2}$$

where n_s and Y_s are the corresponding quantities for the mirror substrate and M_{ij} are the components of M_c [34]. Our mirror substrate is made of BK7 glass with $n_s = 1.50980$.

The resonance frequencies can be determined by plotting the transmission for different wavelengths, and birefringence can be modeled by comparing the calculated resonance frequency with and without a small change in the refractive index.

One important quantity is the fractional splitting $\Delta\nu/FWHM$, which determines the cavity-mediated coupling between the two birefringent modes. Fig. 6.1, 6.2, 6.3, 6.4 present the calculated birefringent splittings with a change in the refractive index $\Delta n \sim 10^{-6} - 10^{-7}$ along one axis. The linewidth and the birefringent splitting are of the same order of magnitude with typically observed values in our cavities used in past experiments [3, 32], suggesting that changes of refractive index in our cavity

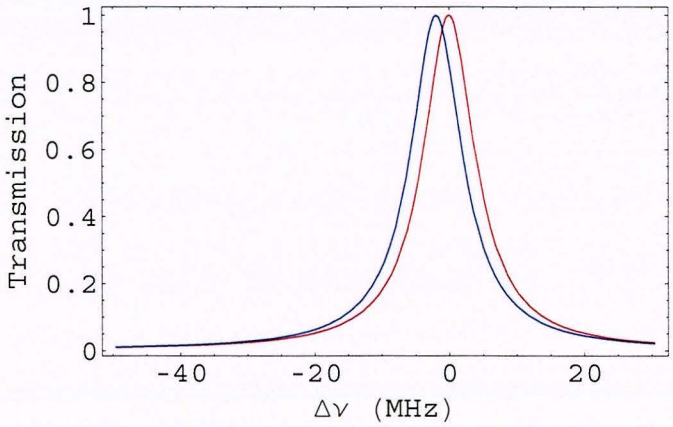

Figure 6.2: Transmission profiles with (blue) and without (red) a change in the refractive index $\Delta n = 5 \times 10^{-7}$. $\Delta\nu$ is the laser detuning from the cavity resonance at 852 nm. The linewidth (FWHM) of the transmission profile is 9.3 MHz and the birefringent splitting is 1.9 MHz, which corresponds to a fractional splitting of 0.2.

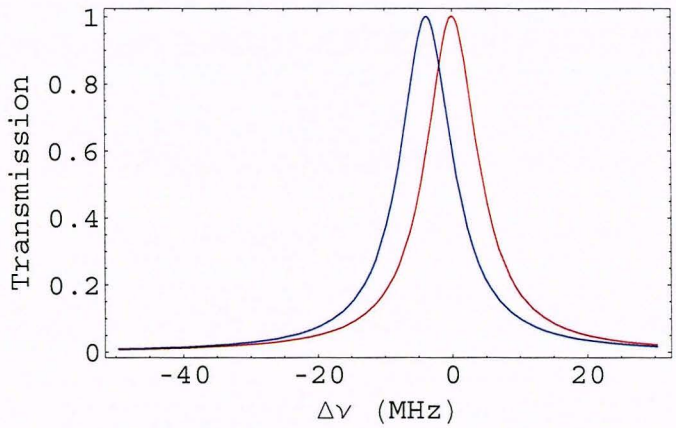

Figure 6.3: Transmission profiles with (blue) and without (red) a change in the refractive index $\Delta n = 1 \times 10^{-6}$. $\Delta\nu$ is the laser detuning from the cavity resonance at 852 nm. The linewidth (FWHM) of the transmission profile is 9.3 MHz and the birefringent splitting is 3.8 MHz, which corresponds to a fractional splitting of 0.4.

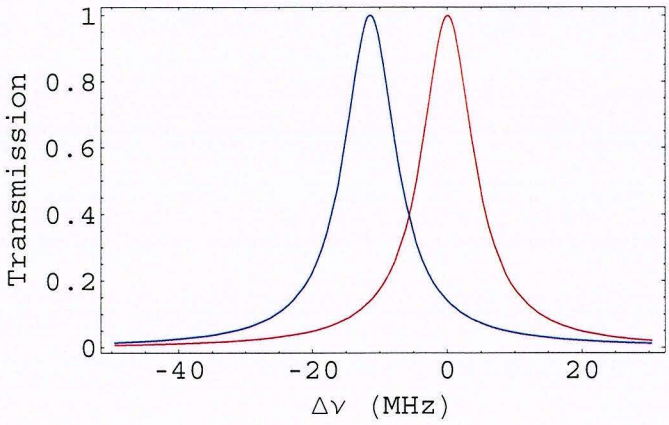

Figure 6.4: Transmission profiles with (blue) and without (red) a change in the refractive index $\Delta n = 3 \times 10^{-6}$. $\Delta\nu$ is the laser detuning from the cavity resonance at 852 nm. The linewidth (FWHM) of the transmission profile is 9.3 MHz and the birefringent splitting is 11.4 MHz, which corresponds to a fractional splitting of 1.2.

mirrors are of similar magnitude. This result is intuitive if we note that any change in the mirror property is amplified by the cavity finesse F. Given $F \sim 10^6$ for our cavity, we would expect a $\Delta n \sim 10^{-7}$ will result in a fractional splitting ~ 0.1.

In our model, cavity birefringence has a nonlinear dependence on the change in the refractive index, which may pose difficulties in active control of its magnitude. However, given that our fractional change in the refractive index is small (10^{-7}–10^{-6}), we can still hope for a linear approximation. Fig. 6.5 shows that the fractional splitting is proportional to Δn, with a proportional constant $\approx 6 \times 10^{-7}$. Although the calculated fractional deviation from linearity is smaller than 10^{-5} for Δn smaller than 10^{-6}, we expect our model to break down well before this level of accuracy is reached. Nonetheless, the result appears promising because a linear relation between cavity birefringence and Δn implies active control is in principle an achievable task.

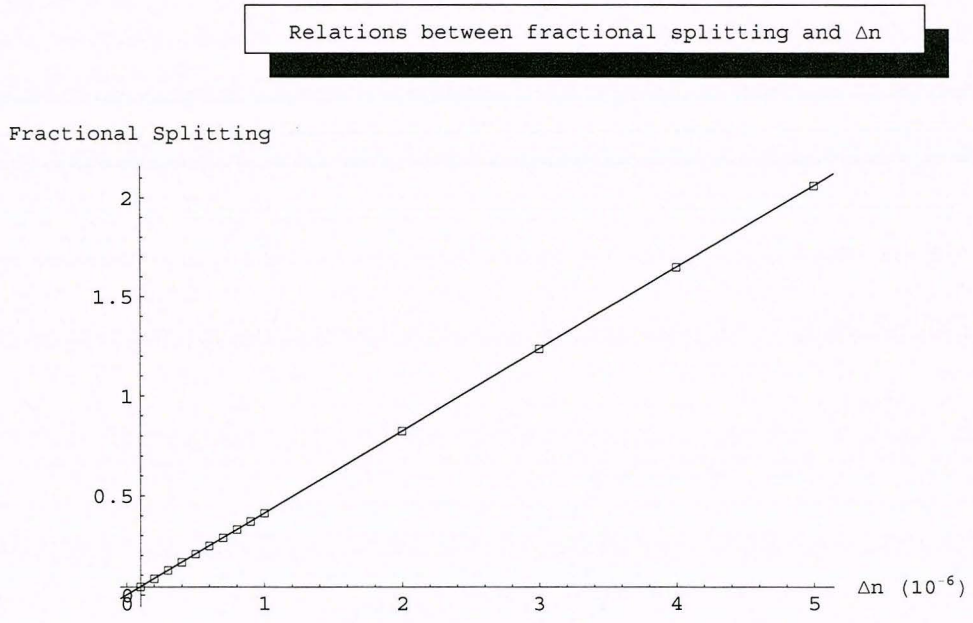

Figure 6.5: Calculated fractional birefringent splitting dependence on change in refractive index. In the limit of small Δn, the fractional splitting can be well approximated linearly with an accuracy better than 10^{-5} for Δn smaller than 10^{-6}.

6.3 Relating Δn to stress in the cavity mirrors

In order to connect between our model on birefringence and experimental results, we must be able to relate the change in refractive index Δn to stress in the cavity mirrors. In my attempt to solve this problem, I employed a linear model in which the refractive indices along orthogonal polarization axes (x,y) are given by

$$n_x = n - C_1\sigma_x - C_2(\sigma_y + \sigma_z) \tag{6.3}$$

$$n_y = n - C_1\sigma_y - C_2(\sigma_z + \sigma_x) \tag{6.4}$$

where n is the refractive index of the unstressed medium, $\sigma_x, \sigma_y, \sigma_z$ are the principal stress components of the medium, and C_1, C_2 are the stress optical coefficients for the extraordinary and ordinary rays respectively [35].

Note that the refractive index increases in response to compressive stress and decreases in response to tensile stress [35]. Since a material usually expands in the directions orthogonal to the direction of compression, the second and third terms in Eq. 6.3, 6.4 have opposite signs. Therefore, the stress optical coefficient $C = C_2 - C_1$ instead of C_1 and C_2 is often found in the literature.

For fused silica, which is one of the materials of the coating on our mirrors, $C = 3.57 \times 10^{-6}$ mm^2/N [36], but I could not locate the stress optical coefficient C for tantalum pentoxide, which is the other material of our mirror coating. I will assume that the stress optical coefficient C for both fused silica and tantalum pentoxide are of the same order of magnitude (i.e. $C \sim 10^{-7}$ mm^2/N). In order to produce a change in the refractive index $\Delta n \sim 10^{-7}$ for a typical fractional birefringent splitting of 0.1, a stress of ~ 0.1 N/mm^2 is required.

In order to model the stress distribution in response to a loading, I did some Finite Element Analysis (FEA) simulations using a program called ABAQUS that I obtained from the Bhattacharya group at Caltech, which will be discussed in detail in Section 6.7.

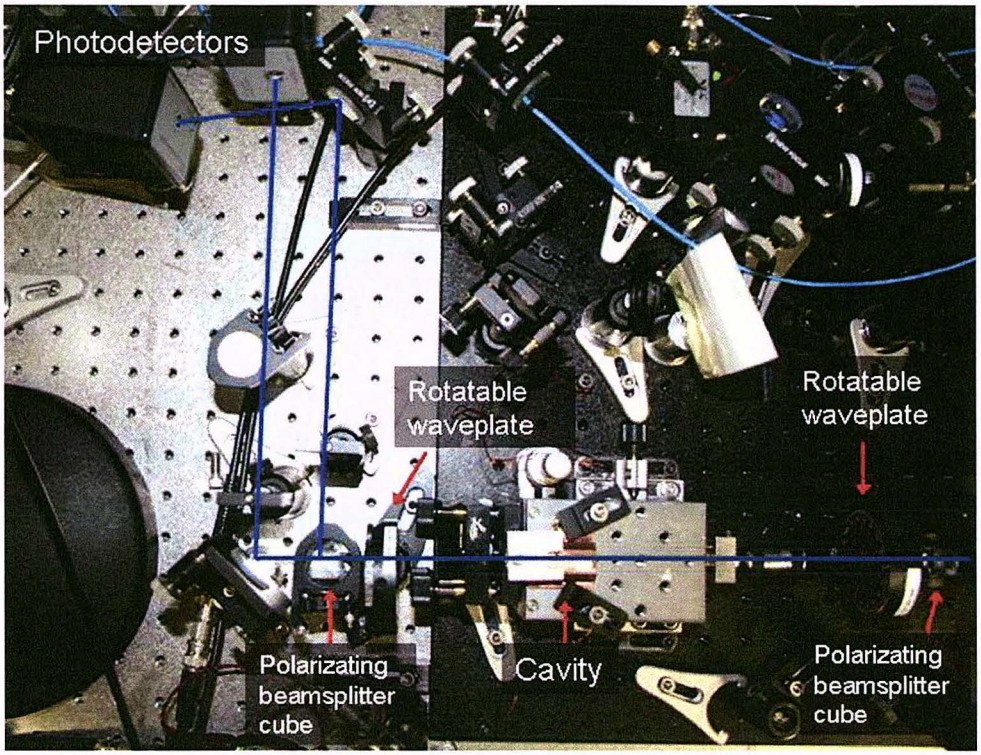

Figure 6.6: A picture of the experimental setup for the measurement of cavity birefringence. The 852 nm beam path is marked as blue.

6.4 Measurements of birefringence

A variety of birefringence-measuring techniques are discussed in Ref. [3], of which we chose two accurate but simple methodes for our measurements.

The two methods we chose are suitable for measuring large birefringent splitting ($\Delta\nu/FWHM > 0.1$), which is the case for the following test cavities. The first method involves the use of linear polarized light. Experimentally, we measure the contrast between power transmissions for on-axis ($\hat{s}, \hat{f}$: the slow and the fast birefringent axes) and off-axis along $(\hat{s}+\hat{f})/\sqrt{2}$ or $(\hat{s}-\hat{f})/\sqrt{2}$ linearly polarized beams. From Eq. 6.5, we can solve for the fractional splitting.

$$\text{Contrast} = \frac{\max - \min}{\max + \min} = \frac{1 - (\Delta\nu/\text{FWHM})^2}{1 + (\Delta\nu/\text{FWHM})^2} \tag{6.5}$$

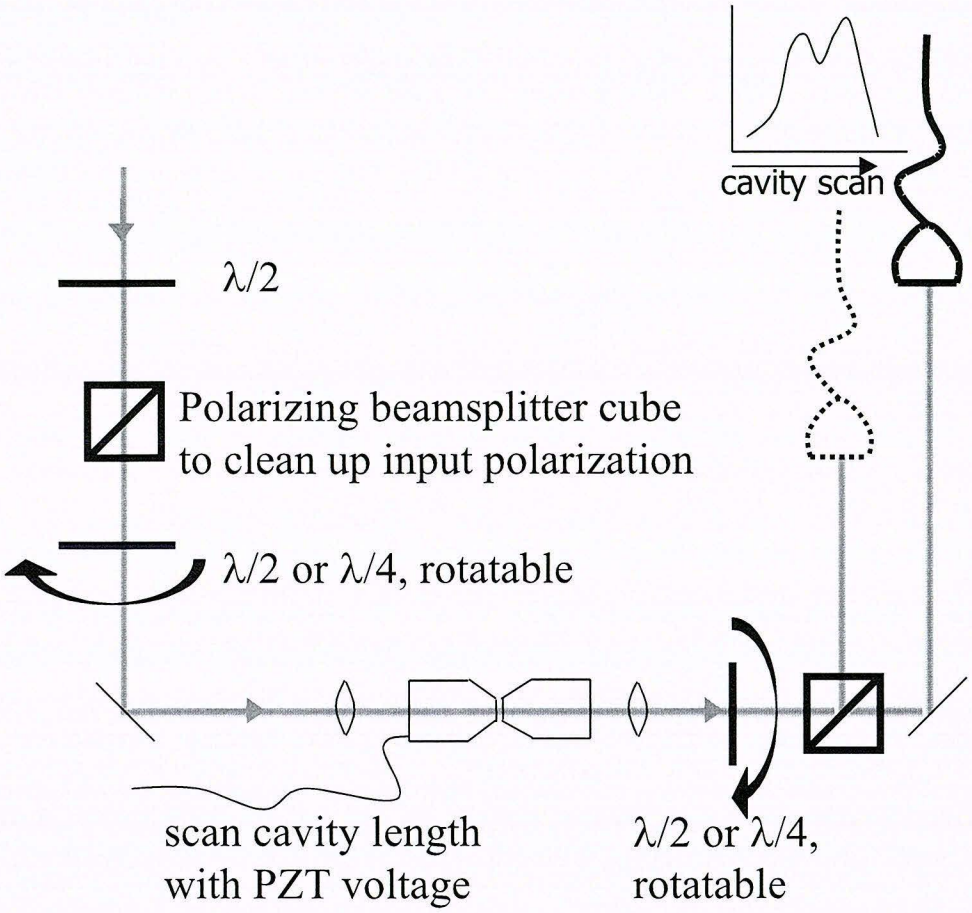

Figure 6.7: A schematic diagram of the experimental setup for the measurement of cavity birefringence [3].

The polarization of the input beam is first cleaned up by a polarizing beamsplitter cube. The beam then passes through a half-waveplate, enters the cavity and passes through another half-waveplate upon exit. The half-waveplate allows us to rotate the polarization of our beam. The transmitted beam from the cavity passes through another polarizing beamsplitter cube so that the two orthogonal polarizations of the output beam can be detected separately (Fig. 6.7, 6.6).

Operationally, we first identify the birefringent axes by rotating both entrance and exit half-waveplates simultaneously so that the axis of the two waveplates are always pointing to the same direction. If the input polarization is on-axis, the polarization is unperturbed by the cavity, and the exit half-waveplate rotates it back to the original direction; if the input polarization is off-axis, the polarization of the beam from the exit waveplate will be perturbed. In practice, we maximize the ratio of the signal passing straight through to that being reflected through 90° by the output polarizing beamsplitter cube. We record the transmission peak passing straight through the cube as our *max* in Eq. 6.5. Then we rotate the entrance waveplate by 45° and then rotate the exit waveplate to maximize the transmission peak contrast between the signals on the two detectors. This maximum transmission peak is our *min* in Eq. 6.5.

The second method involves the use of circularly polarized light. The experiment setup is identical to that in the first method, except a quarter-waveplate is used before the cavity entrance instead of a half-waveplate. It can be shown that the power transmission T is given by

$$T = T_0 \left(\frac{cos^2\theta}{\kappa^2 + (\nu + \delta)^2} + \frac{sin^2\theta}{\kappa^2 + (\nu - \delta)^2} + \frac{2\kappa\delta sin(2\theta)}{(\kappa^2 + (\nu + \delta)^2)(\kappa^2 + (\nu - \delta)^2)} \right) \quad (6.6)$$

where T_0 is the peak transmission, κ is the linewidth of each birefringent mode, δ is half the birefringent splitting, ν is the detuning of the incoming beam from the center of the cavity resonance and θ is the angle between the axis of the waveplate and the one of birefringent axis [32].

The birefringent splitting can be determined by fitting the transmission spectrum

to Eq. 6.6.

6.5 Measuring change in birefringence with known external loading

In our first attempt to actively induce cavity birefringence, I suggested measuring the birefringent splittings upon known external loading and Dal implemented the idea by placing a known weight on a three-point support, one point of which is our cavity mirror (Fig. 6.8). We tried to distribute weight along the three points as even as possible, but we estimated it was only accurate up to $\sim$ 10% for our setup. To add another level of complexity, our cavity became misaligned if we simply applied the external loading. Toby Burrows reported a similar phenomenon when he attempt to induce birefringence by streeing the cavity with a screw [31]. We overcame this difficulty by preloading our cavity mirror with a wire (Fig. 6.9). We estimated the preloading to be $\sim$ 100 N, but we did not have a method to accurately measure the magnitude of the preloading. Moreover, we did not know whether the preloading changed as the external loading varied. Although we expected the preloading wire would become looser as the mirror is farther compressed, more tests are needed to confirm any of these hypotheses.

Fig. 6.10 shows that the fractional birefringence decreased as the external loadings increased, an apparent contrary to the predication of our simple model. However, we can understand the result by noting the observed rotation of the birefringence axes. As shown in Fig. 6.11, the birefringent axis was rotated by 90 ° as the loading increased from zero to its maximum value. At the same time, the birefringent splitting decreased from its maximum value to almost zero. These two observations suggested that birefringence caused by the stress from preloading was dominatant at small loading and was replaced slowly birefringence caused by the stress from the known external loading, as the external loading increased. Moreover, the principal axes of these two causes of birefringence were orthogonal to each other, and therefore the two factors

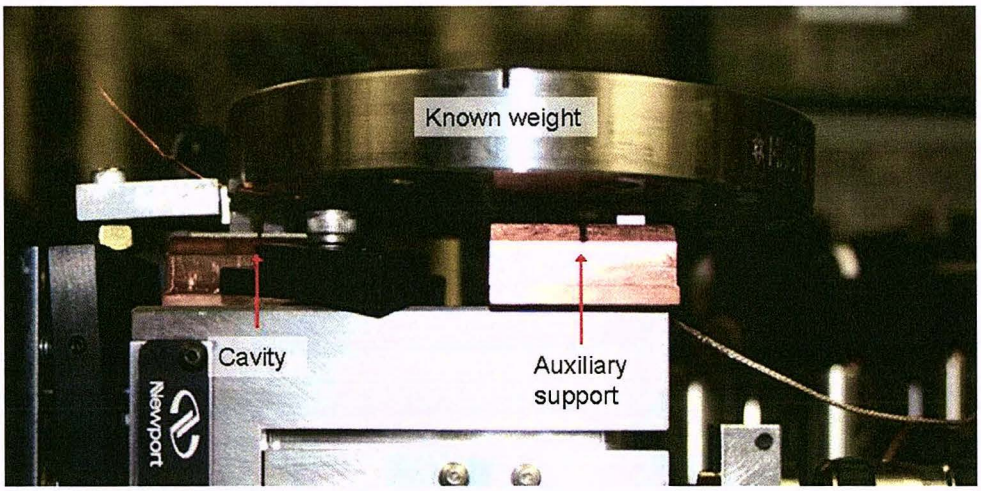

Figure 6.8: In our first attempt to actively induce cavity birefringence, we placed a known weight on a three-point support, one point of which is our cavity mirror.

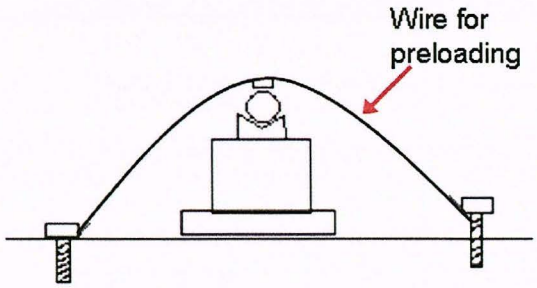

Figure 6.9: In order to avoid misalignment of the cavity upon application of external loading, we preloaded our cavity with a wire [37].

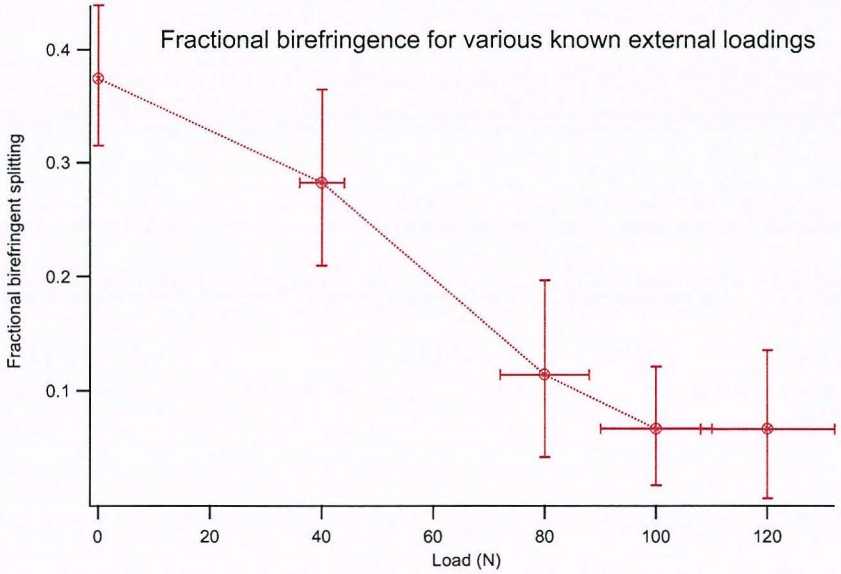

Figure 6.10: Fractional birefringence for various known external loadings.

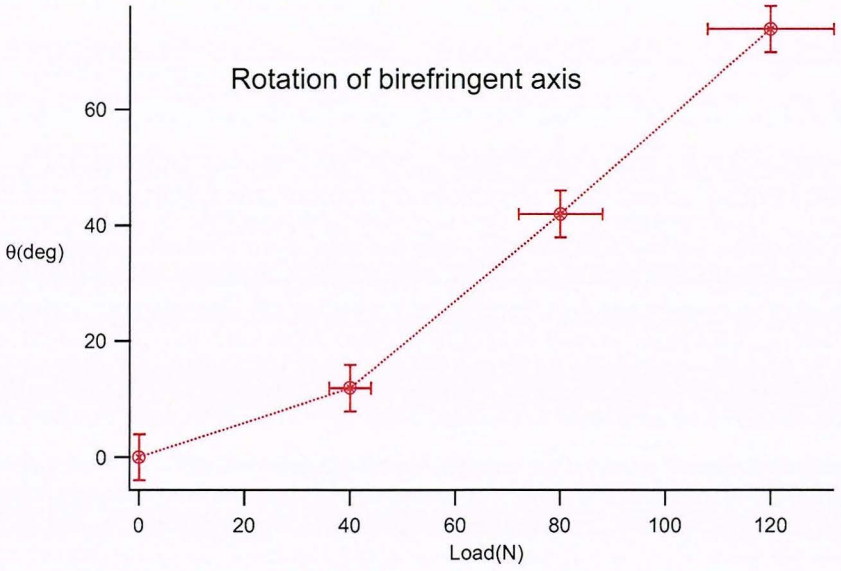

Figure 6.11: Rotation of the birefringence axis at various external loading. θ is the orientation of the birefringence axis at a particular loading measured from the birefringence axis at at zero loading.

canceled out each other. A model for the addition of stress-induced birefringent splittings has yet to be developed. Nonetheless, the results appeared promising as we reduced the birefringence, a first step toward controlling birefringence.

6.6 First step toward minimization

In order to further our investigation of actively induced birefringence, Dal designed and built a test mirror mount that can induce stress on the mirror with a piezo (Fig. 6.12). In this setup, we preloaded the mirror with set screws and induced stress along two orthogonal directions on the mirror with piezos. Although it is in principle helpful to calibrate the piezos as pressure gauges, we did not carry out the calibration due to hysteresis. Therefore, we did not know how much pressure was exerted on the mirror.

Fig. 6.13 shows the fractional birefringent splittings at various piezo voltages. We also did not observe any change in the orientation of the birefringent axis as the piezo voltage increased from zero to its maximum value. Note that we only used the piezo along the vertical direction to stress the mirror in the measurement because the piezo along the horizontal direction was malfunctioning. At piezo voltage of about 50 V, the TEM_{00} which we have beening observing overlapped with one of its neighboring higher order spatial mode, as we verified by looking the cavity output with a infrared-sensitive camera. Hence, the peak near 50 V was actually due to a superposition of two spatial modes, which are extinguishable by the power transmission signal. Except for this peak, the fractional birefringent splitting increased approximately linearly with the piezo voltage, in agreement with our mode. If the piezos were calibrated as pressure gauges, we could compare the fitted slope with a calculated value in our model.

We also noticed that it was easier for this test cavity to draft out of resonance, probably because it was less mechanically stable. Therefore, we would like to seek a more mechanically stable structure with which to stress our mirrors.

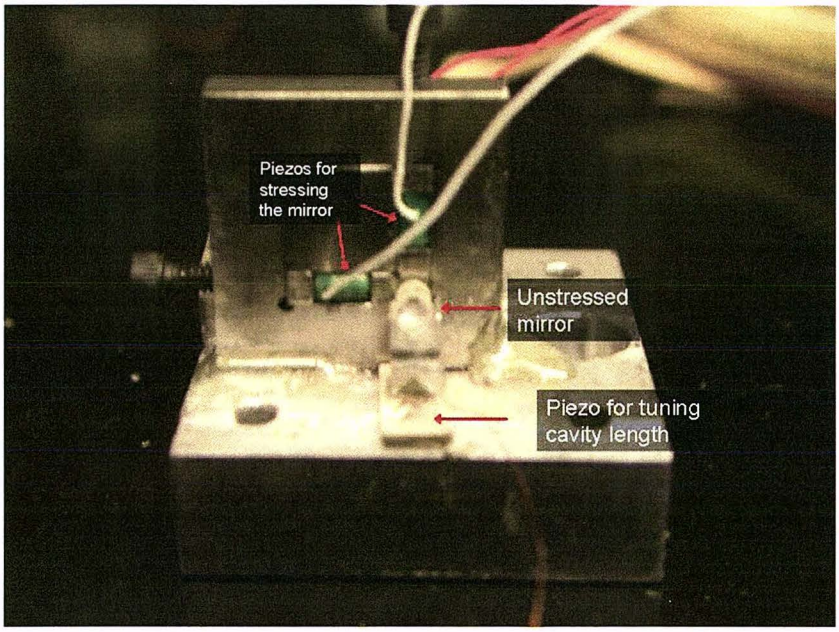

Figure 6.12: A test mirror mount that has two piezos to induce stress on the mirror. The mirror was preloaded with set screws in order to avoid misalignments at various loadings. Due to hysteresis, we did not calibrate the piezos as pressure gauges, although it is possible to do so in principle. Therefore, we did not know how much pressure was exerted on the mirror.

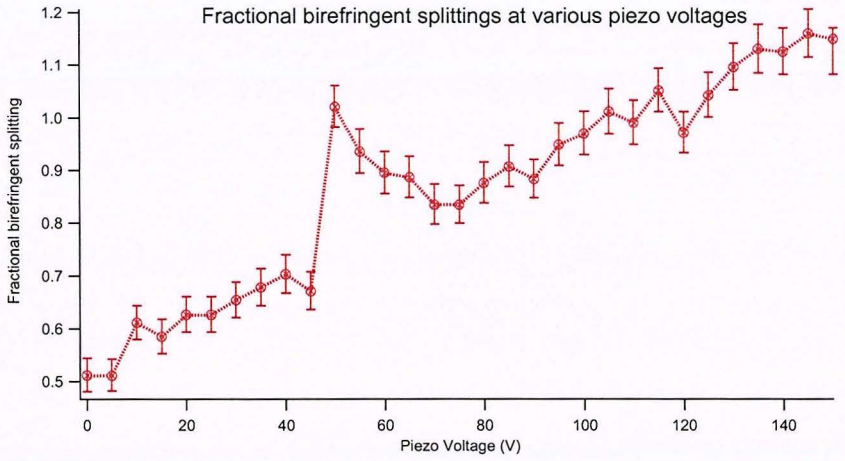

Figure 6.13: Fractional birefringent splittings at various piezo voltages. The peak at 50 V was due to the superposition of the TEM_{00} mode and one of its neighboring higher order spatial mode. Except for this peak, the fractional birefringent splitting increased linearly with the piezo voltage.

6.7 Second step toward minimization

In attempt to find a method to induce stress our mirrors inside the vacuum chamber, I suggested stressing the cavity mirror with an expansion-mode piezo on the V-block that holds the mirror (Fig. 6.14). We built a prototype of this mirror mount and attempted to induce cavity birefringence. I also did a Finite Element Analysis (FEA) simulation using a program called ABAQUS that I obtained from the Bhattacharya group at Caltech, as my first attempt to model cavity birefringence.

In my FEA simulations, I sliced the cavity mirror into elements of length ~ 100 μm. Stress can only be applied to an element at a node (where two elements join) and along the axis of the element. The program then simulates the resultant system of linear differential equations (Newton's second law) numerically. The boundary conditions in the simulations were that the mirror is fixed along the edge E1 and a uniform shear-stress is applied along the edge E2 pointing outward from the center (Fig. 6.15, 6.16).

According to the simulation, a 10 N force from the piezo is needed to induce

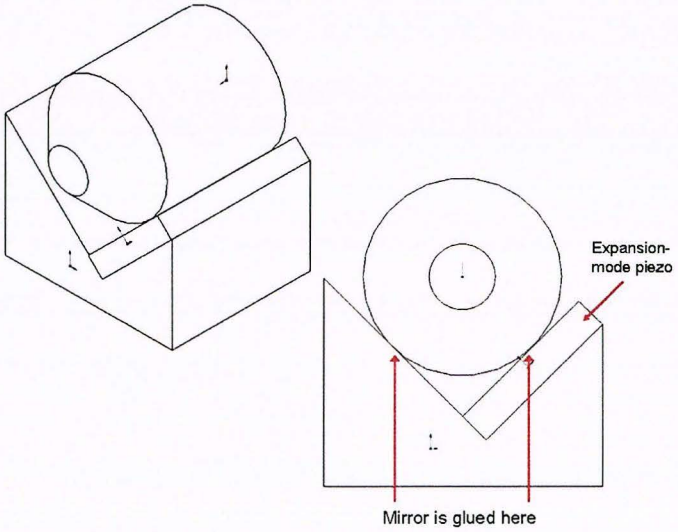

Figure 6.14: A V-block with an expansion-mode piezo that can induce stress on the cavity mirror. Caburn H27DUHV epoxy was applied along the entire length of the mirror substrate for attaching the mirror to the V-block and the piezo.

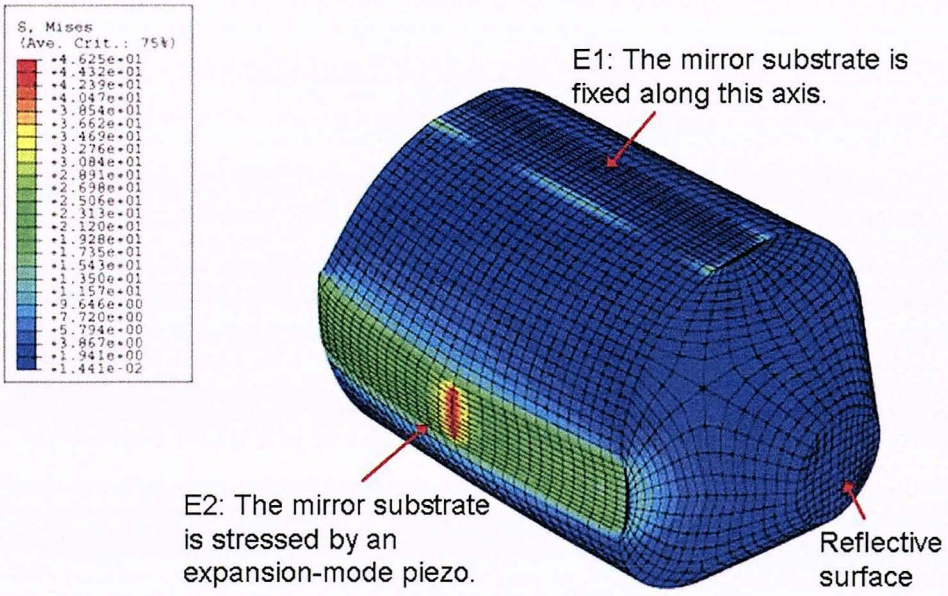

Figure 6.15: FEA-modeled stress distribution on the cavity mirror: side view. The deformation is magnified by 1500 times in the figure for clarity. The color code represents the level of Von Mises stress in N/mm^2.

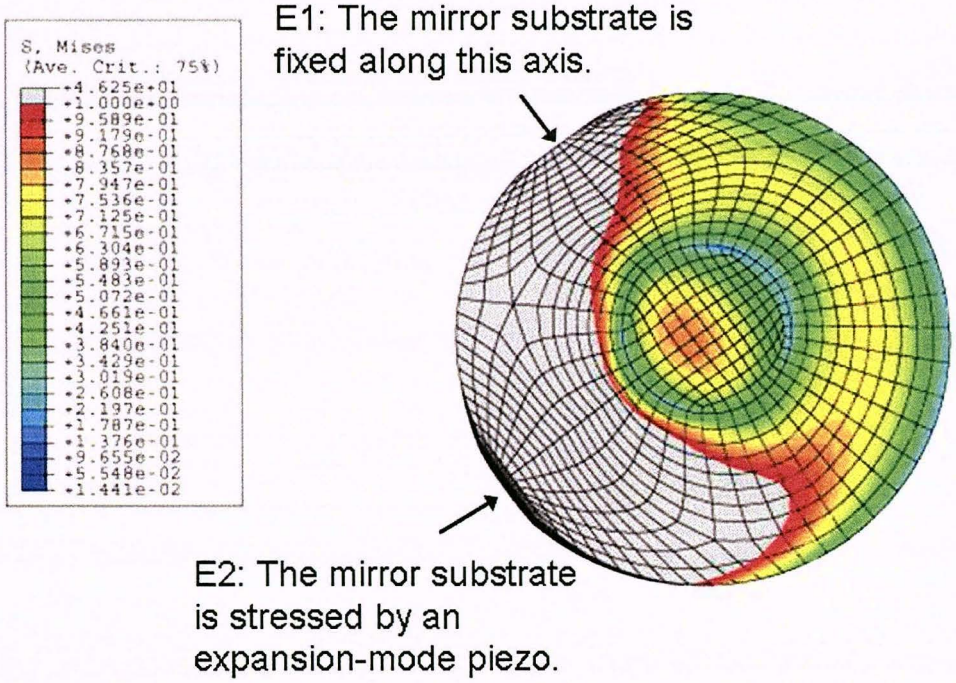

Figure 6.16: FEA-modeled stress distribution on the cavity mirror: front view. The deformation is magnified by 1500 times in the figure for clarity. The color code represents the level of Von Mises stress in N/mm^2.

an Von Mises stress of ~ 0.1 N/mm^2 required for a typically observed fractional birefringent splitting of 0.1 (Section 6.1). Von Mises stress (σ_v) is defined as $\sigma_v = sqrt[(\sigma_1 - \sigma_2)^2 + (\sigma_2 - \sigma_3)^2 + (\sigma_3 - \sigma_1)^2]/2$ with σ_i the principal stress and is commonly used in FEA. Ideally, we would calculate the stress and hence the change in reflective index in each layer within the coating stack individual in order to calculate the birefringent splitting. In practice, due to limited computing resources, I assumed the stress within each layer of the coating was identical to the stress in the same region of a single block of fused silica. Since the blocked force (i.e. the maximum force that the piezo can provide) is $\sim$ 100 N, we expect this design is able to actively induced observable birefringence even if the stress coupling efficiency between the piezo and the mirror substrate is reduced by the glue.

We built a prototype of the cavity with the piezoelectric V-block and made some preliminary measurements on birefringence (Fig. 6.17). The spectrum shows a dependence of birefringence on the piezo voltage. The transmission was taken with an injection of circularly polarized light. The laser detuning was provided by small amplitude vibrations of the cavity mirrors. In principle, we can calibrate the laser detuning by putting on known sidebands with an electro-optic modulator (EOM), but the setup broke before we could perform further measurements. We attempted to fit the transmission spectra to Eq. 6.6 with a constant background, but were unable to obtain a reasonable fit. One possible caused was the ellipticity of the polarization of our beam was too high to be well-approximated by circular polarization, which is described by Eq. 6.6. The other possibility is that the background noise of our photodiode increases with intensity. However, more tests are required to determine the exact causes. Instead, we estimated the splittings by comparing the transmission spectra with a series of graphs of birefringent splitting calculated using the transfer matrix formalism (Section 6.1). The fractional splittings increased from ≈ 0.3 to ≈ 1 as the piezo voltage increased from 0 V to 300 V. Since we did not know how much force the piezo was exerting on the mirror substrate, we were unable to compare the experimental results with our simulations quantitatively.

We attempted to reproduce the results by building three additional test cavities

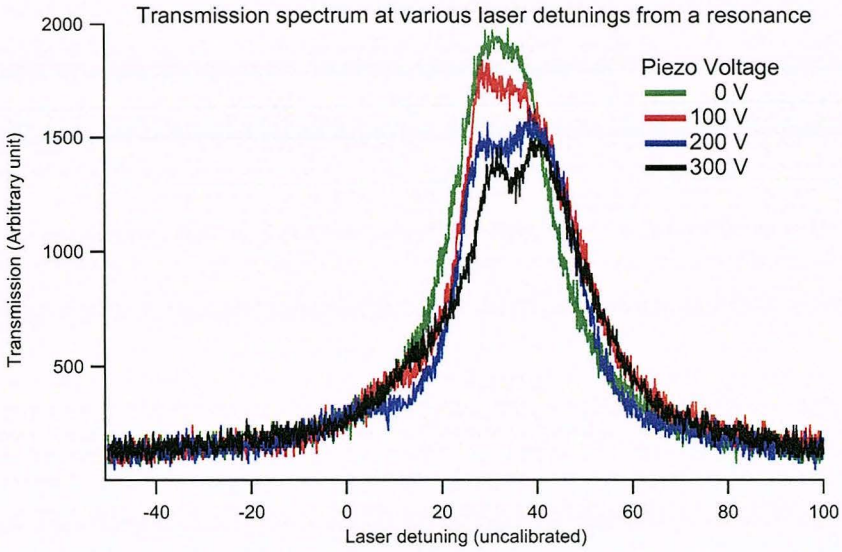

Figure 6.17: Preliminary birefringence data from the piezoelectric V-block. The transmission was taken with an injection of circularly polarized light. The laser detuning was provided by small amplitude vibrating of the cavity mirrors. In principle, we can calibrate the laser detuning by putting on known sideband with an electro-optic modulator (EOM), but the setup broke before we could perform further measurements.

with the piezoelectric V-blocks, but we could not induce birefringence on all three cavities. We suspect that the functioning of this design depends on the special curing condition of the epoxy, but more tests are needed to confirm our hypothesis. Nonetheless, this test marked our first attempt to design a mirror-stress-inducing structure that can be incorporated into the vacuum system.

6.8 Limitations of our model

There are five major limitations on our simple model of cavity birefringence. First, we do not account for prior stress in the mirrors, which is important if we preload our cavity mirrors or if we want to minimize birefringence. Second, our model does not account for the direction of the principal birefringent axes, which is critical for interpretations of some the above results. Third, our FEA simulations do not account for the interactions with the 40-layer stack of coating and between the mirror substrate and its boundary conditions in the presence of the epoxy. Although the modelings of this kind of interactions are routinely done in industrial design, the computing resources required will be beyond the reach of our group in the foreseeable future. Fourth, we need to account for the birefringent effect for higher order spatial modes. Fifth, we would need to understand how to obtain a feedback signal to control birefringence from a locked cavity. Definitely, more tests and detail studies are required before we can actively control cavity birefringence.

Chapter 7

Outlook and Conclusions

We demonstrated actively induced cavity birefringence by stressing the mirrors with piezoelectric materials, although we had little control over both stress and induced birefringence.

In the near future, we should attempt to stress the cavity mirrors along two orthogonal directions, perhaps with the setup described in Section 6.6 or its modified versions. We would like to determine whether it is feasible to cancel birefringence completely by stressing our cavity mirrors along two orthogonal directions and to learn about the achievable level of control.

In the medium term, we should design structures that can be incorporated into a vacuum chamber. Because of the requirements imposed by beam access around the cavity and mechanical stability of the system, we may only be able to stress our mirrors along two independent but nonorthogonal axes. Since it is time-consuming to build a prototype setup, the use of finite element analysis simulations to aid the design and development process is recommended. I have done initial finite element analysis simulations to model the effect of stres on mirror birefringence.

In the long term, we need to understand how to obtain a feedback signal to control birefringence from a locked cavity.

Since canceling or minimizing cavity birefringence requires better understanding of our system, it is likely that we will be able to increase birefringent splittings inside the vacuum chamber before we can minimize them.

Bibliography

[1] C. Cohen-Tannoudji, B. Diu, and F. Laloe. *Quantum Mechanics Volume I.* Hermann, Paris, France, 1977.

[2] J. Preskill. Lecture notes for physics 229: Quantum information and computation. Lecture Notes, 1997.

[3] T. Lynn. *Measurement and Control of Individual Quanta in Cavity QED.* PhD thesis, California Institute of Technology, 2003.

[4] R.J. Thompson, G. Rempe, and H.J. Kimble. Observation of normal-mode splitting for an atom in an optical cavity. *Physical Review Letters*, 68:1132, 1992.

[5] H. Mabuchi, Q.A. Turchette, M.S. Chapman, and H.J. Kimble. Real-time detection of individual atoms falling through a high-finesse optical cavity. *Optics Letters*, 21:1393, 1996.

[6] H. Walther, B.T.H. Varcoe, B. Englert, and T. Becker. Cavity quantum electrodynamics. *Reports on Progress in Physics*, 69:1325, 2006.

[7] A. Blais, R. Huang, A. Wallraff, S.M. Girvin, and R.J. Schoelkopf. Cavity quantum electrodynamics for superconducting electrical circuits: an architecture for quantum computation. *Physical Review A*, 69:062320, 2004.

[8] K. Libbrecht. Fabry-perot cavities and fm spectroscopy. Lecture Notes, 2005.

[9] A.E. Siegman. *Lasers.* University Science Books, Sausalito, CA, 1986.

[10] G. Rempe, R.J. Thompson, H.J. Kimble, and R. Lalezari. Measurement of ultralow losses in an optical interferometer. *Optics Letters*, 17:363, 1992.

[11] E.T. Jaynes and F.E. Cummings. Comparison of quantum and semiclassical radiation theories with application to the beam maser. *IEEE proceedings*, 51:89, 1963.

[12] H. Carmichael. *An Open Systems Approach to Quantum Optics*. Springer-Verlag, Heidelberg, Germany, 1993.

[13] J. McKeever, J.R. Buck, A.D. Boozer, A. Kuzmich, H.C. Nagerl, D.M. Stamper-Kurn, and H.J. Kimble. State-insensitive cooling and trapping of single atoms in an optical cavity. *Physical Review Letters*, 90:13, 2003.

[14] H. Metcalf and P. Van der Straten. *Laser Cooling and Trapping*. Springer-Verlag, New York, NY, 1999.

[15] C.J. Hood, T.W. Lynn, A.C. Doherty, A.S. Parkins, and H.J. Kimble. The atom-cavity microscope: single atoms bound in orbit by single photons. *Science*, 287:1457, 2000.

[16] P.W.H. Pinkse, T. Fischer, P. Maunz, and G. Rempe. Trapping an atom with single photons. *Nature*, 404:365, 2000.

[17] S. Nussmann, M. Hijlkema, B. Weber, F. Rohde, G. Rempe, and A. Kuhn. Submicron positioning of single atoms in a microcavity. *Physical Review Letters*, 95:173602, 2005.

[18] J. Sauer. *Cold Atoms Manipulation for Quantum Computing and Control*. PhD thesis, Georgia Institute of Technology, 2004.

[19] A. Boca, R. Miller, K.M. Birnbaum, A.D. Boozer, J. McKeever, and H.J. Kimble. Observation of the vacuum rabi spectrum for one trapped atom. *Physical Review Letters*, 93:233603, 2004.

[20] J.I. Cirac, P. Zoller, H.J. Kimble, and H. Mabuchi. Quantum state transfer and entanglement distribution among distant nodes in a quantum network. *Physical Review Letters*, 78:3221, 1997.

[21] L.M. Duan and H.J. Kimble. Scalable photonic quantum computation through cavity-assisted interactions. *Physical Review Letters*, 92 (12):127902, 2004.

[22] R. Miller, T.E. Northup, K.M. Birnbaum, A. Boca, A.D. Boozer, and H.J. Kimble. Trapped atoms in cavity qed: coupling quantized light and matter. *Journal of Physics B: Atomic, Molecular, and Optical Physics*, 38:S551, 2005.

[23] J. Buck. *Cavity QED in Microsphere and Fabry-Perot Cavities.* PhD thesis, California Institute of Technology, 2003.

[24] N. Harris. *Modern Vacuum Practice.* Mcgraw-Hill, Dallas, TX, 2005.

[25] K.M. Birnbaum. *Cavity QED with Multilevel Atoms.* PhD thesis, California Institute of Technology, 2005.

[26] J.P. Bacher, C. Benvenuti, P. Chiggiato, M.P. Reinert, S. Sgobba, and A.M. Brass. Thermal desorption study of selected austenitic stainless steels. *Journal of Vacuum Science & Technology A*, 21(1):167, 2002.

[27] K Jousten. Thermal outgassing. CERN Technical Notes, 2005.

[28] Kaushik Bhattacharya, 2005. Private communication.

[29] C. Hood. *Real-time Measurement and Trapping of Single Atoms by Single Photons.* PhD thesis, California Institute of Technology, 2000.

[30] K. Birnbaum. Making a cavity. Technical Notes, 2001.

[31] T. Burrows. Active control of birefringence in optical cavities for cavity qed. Caltech Summer Undergraduate Research Fellowships Final Report, 2005.

[32] A. Boca. *Experiments in Cavity QED: Exploring the Interaction of Quantized Light with a Single Trapped Atom.* PhD thesis, California Institute of Technology, 2005.

[33] L.M. Duan, A. Kuzmich, and H.J. Kimble. Cavity qed and quantum-information processing with hot trapped atoms. *Physical Review A*, 67:032305, 2003.

[34] C.J. Hood, H.J. Kimble, and J. Ye. Characterization of high-finesse mirrors: Loss, phase shifts, and mode structure in an optical cavity. *Physical Review A*, 64:033804, 2001.

[35] W. Hermann, M. Hutjens, and D.U. Wiechert. Stress in optical waveguides. 3: Stress induced index change. *Applied Optics*, 28 (11):1980, 1989.

[36] W. Primak and D. Post. Photoelastic constants of vitreous silica and its elastic coefficient of refractive index. *Journal of Applied Physics*, 30 (5):779, 1959.

[37] Dalziel Wilson, 2006. Private communication.